Durham University

Durham E-Theses

A flexible Temperature Sensor Based on a Two-Terminal Thin-Film Organic Device

Xuyan Wu

How to cite:

Wu, Xuyan (2026) A flexible Temperature Sensor Based on a Two-Terminal Thin-Film Organic Device. Masters thesis, Durham University.

Use policy

The full-text may be used and/or reproduced, and given to third parties in any format or medium, without prior permission or charge, for personal research or study, educational, or not-for-profit purposes provided that:

- a full bibliographic reference is made to the original source
- a https://etheses.durham.ac.uk/id/eprint/16658/ is made to the metadata record in Durham E-Theses
- the full-text is not changed in any way

The full-text must not be sold in any format or medium without the formal permission of the copyright holders.

Please consult the full Durham E-Theses policy for further details.

Academic Support Office, The Palatine Centre, Durham University, Stockton Road, Durham, DH1 3LE
e-mail: e-theses.admin@durham.ac.uk Tel: +44 0191 334 6107
https://etheses.durham.ac.uk

A flexible Temperature Sensor Based on a Two-Terminal Thin-Film Organic Device

Xuyan Wu

A Thesis presented for the degree of

Master by Research

Department of Engineering

Durham University

United Kingdom

October 2025

Abstract

Flexible temperature sensors are increasingly important for wearable and biomedical applications, owing to their light weight, conformability, and potential for real-time monitoring. Organic semiconductors, with their solution process ability and tunable electronic properties, provide a compelling route towards such devices. Among donor-acceptor copolymers, PCDTPT[poly[(4,4-bis(2-ethylhexyl)cyclopenta-[2,1-b:3,4-b′]dithiophene)-2,6-diyl-alt-[1,2,5]thiadiazolo[3,4-c]pyridine]] has attracted particular attention for its high carrier mobility. However, its temperature-dependent electrical behaviour in two-terminal devices, particularly as a function of polymer concentration on flexible substrates, has not been systematically investigated.

Therefore, the central research question addressed in this work is: How does polymer concentration affect the structural and temperature-dependent electrical behaviour of PCDTPT thin films fabricated on flexible substrates?

This study investigates the thermal-electrical properties of PCDTPT thin films fabricated through spin coating onto PET and glass substrates with Ag and Au electrodes, respectively. Film morphology and interfacial quality were characterised by atomic force microscopy (AFM) and X-ray reflectivity (XRR), revealing high-

quality layer stacking and distinct layer boundaries. As the temperature rises from 25°C to 85°C, a clear decrease in resistance was observed, suggesting that charge transport is influenced by thermally activated processes. A comparative analysis of the three devices fabricated with PCDTPT films at different concentrations revealed that the device prepared using a 10 mg/mL solution exhibited comparatively lower room-temperature resistance and a more consistent temperature-dependent response than those prepared from 5 mg/mL and 15 mg/mL solutions.

Declaration

The work in this thesis is based on research carried out at the Department of Engineering, Durham University, United Kingdom. No part of this thesis has been submitted elsewhere for any other degree or qualification and it is all my own work unless referenced to the contrary in the text.

Copyright © 2025 by Xuyan Wu.

"The copyright of this thesis rests with the author. No quotations from it should be published without the author's prior written consent and information derived from it should be acknowledged".

Acknowledgements

The research presented in this thesis would not have been possible without the constant support of my parents, whose encouragement and guidance have been invaluable. I am also grateful to my friends for their patience and assistance throughout the course of this work. I would like to take the opportunity to thank them all for their aid, time and patience.

At the Department of Engineering at the University of Durham, I would like to express my gratitude to my supervisors, Dr. Iddo Amit and Dr. Del Atkinson, for their careful guidance and constructive advice during this project. Their insight and expertise have been essential to the progress and completion of this research.

I would like to express my sincere gratitude to the laboratory technicians and colleagues for providing training in the safe use of laboratory equipment and their detailed guidance in many facilities at the cleanroom.

I would also like to thank my office colleagues for their generous assistance in both experimental procedures and academic discussions. Their willingness to share knowledge and overcome challenges with me made the research process more collaborative and enriching.

Finally, I offer my thanks to all my other colleagues at Durham whose support has very much helped the completion of my work.

Contents

List of Figures

List of Tables

CHAPTER 1

Introduction and Structure of Thesis

1.1 Introduction

Over decades of development, traditional rigid silicon-based temperature sensors have presented excellent accuracy and robustness even under extreme conditions. However, as electronics evolve toward flexibility and integration with daily life, the demand for adaptable and flexible electronics has expanded rapidly [1, 2]. The limitations of traditional sensors, such as rigidity [3] and brittleness [4], have stimulated growing interest in organic materials and devices, particularly those featuring mechanical flexibility [5], structural versatility, and cost-effective processing [6].

Flexible sensors are electronic devices fabricated through micro- and nano- processing of flexible materials based on their bendability, stretchability, and wearabil-

ity, or even the ability to be freely bent or folded [7]. Organic semiconductors are especially attractive because they not only achieve excellent temperature-sensing performance of traditional temperature sensors, but also provide additional advantages, including biocompatibility [8], combined with the mechanical flexibility and stretchability required to conform to curved or irregular surfaces [9–12], as well as suitability for large-area, solution-based processing [10, 13, 14].

Flexible organic sensors can detect a wide range of stimuli, such as temperature, pressure, and humidity. Among these, temperature sensing has emerged as a particular focus [15], especially in health monitoring [16], robotics, and environmental sensing [17]. The rapid advancement of electronic skin has further highlighted the need for temperature sensors that are not only accurate but also flexible, stretchable, and capable of spatially resolved thermal mapping for practical applications [18]. Beyond direct physiological monitoring, temperature sensing also plays a key role in the reliable interpretation of other physical parameters, such as pressure, humidity, and gas concentration, which are often temperature-dependent [19]. Without compensating for thermal changes, precise sensing in these factors becomes unreliable [20].

In terms of human body temperature monitoring, flexible thermal sensors have gained increasing attention in the medical field, as body temperature carries essential physiological information related to metabolism, emotional state, and infections caused by viruses or bacteria. When attached to the skin, these flexible and high-performance temperature sensors can continuously monitor body temperature, supporting the early diagnosis and prevention of disease [21]. Compared with tra-

ditional rigid thermometers, flexible sensors offer improved accuracy and real-time responsiveness in body temperature monitoring [22].

In the measurement of object and system temperatures, flexible temperature sensors have also found wide applications, such as robotic skin, prosthetic devices, wearable electronics, and energy-storage systems. In robotics and prosthetics, flexible temperature sensors embedded in artificial skin enable machines and assistive devices to acquire thermal signals similar to biological systems, realising their adaptability and interaction with humans [11,23,24]. For energy-storage components, flexible sensors can conform to battery surfaces, providing real-time thermal feedback to prevent overheating, mitigate fire hazards, and improve thermal management. Such monitoring also assists in predicting battery lifetime and evaluating performance in next-generation energy systems [25–27].

1.2 Motivation

Although significant progress has been made in the development of organic temperature sensors through strategies such as doping, grain-boundary engineering, and device architecture optimisation, the potential of pristine PCDTPT as a thermally responsive material in passive sensing applications has been insufficiently investigated.

Based on these observations, the material focus of this study is the organic semiconductor polymer PCDTPT. The overall aim is to investigate the relationship between polymer concentration and its electrical behaviour, and to further understand how different concentrations influence the electrical performance as temperature in-

creases. The conductivity of organic semiconductors can be affected by multiple processing variables. For instance, as temperature rises, charge carriers acquire sufficient energy to hop between localised states, leading to enhanced conductivity [28, 29]. However, this behaviour also strongly depends on the concentration of the polymer, which controls the density of available transport pathways [30, 31]. A detailed experimental analysis of this concentration dependence is presented in Chapter 4, Section 4.3.

To address this gap, this study aims to investigate the potential of pristine PCDTPT applied in flexible temperature sensors by examining the thermal response of intrinsic PCDTPT with different concentrations deposited on flexible substrates. Through X-ray reflectivity (XRR) and temperature-dependent resistance measurements, the influence of film structure, interfacial quality, and concentration on thermal sensitivity as well as electrical behaviour is analysed. The results provide new insights into the charge transport behaviour of organic semiconductors, highlighting the role of polymer concentration in governing resistance, activation energy, and temperature-dependent response, and demonstrating the applicability of PCDTPT in next-generation flexible temperature sensors.

1.3 Outline of Remaining Chapters

This section briefly details the contents of the forthcoming chapters in the thesis.

Chapter 2 provides the theoretical background necessary for this study. It begins with a background review of rigid temperature sensors and the rise of flexible ones. Then introduces the fundamental physics of inorganic semiconductors,

followed by the principles of organic semiconductors, including the carrier transportation mechanism. Finally, temperature sensing mechanisms are discussed to connect material properties with device performance.

Chapter 3 presents the experimental methodology, including the preparation of PCDTPT polymer solutions at three different concentrations, thin-film deposition on flexible substrates, and the setup of temperature-dependent electrical measurements. Structural characterisation using X-ray reflectivity (XRR) is also described.

Chapter 4 presents the experimental results, with focus on the influence of polymer concentration, interfacial quality, and film structure on the thermal response and conductivity changes.

Chapter 5 provides the overall conclusions of the study and offers suggestions for future research directions.

CHAPTER 2

Semiconductors: Physical Principles and Sensing Mechanisms

2.1 Introduction

In this chapter, the fundamental concepts of temperature sensing in semiconductors are introduced, with emphasis on the basic theories that provide the foundation for analysing the experimental results presented later in this thesis. To place this study within the broader context of flexible electronics, the discussion begins with the basic theories of inorganic and organic semiconductors to establish the necessary theoretical background. Then, a brief review of rigid temperature sensors are introduced, followed by an overview of the emergence of flexible sensors. Finally, the operating mechanisms of temperature sensors are also reviewed.

2.2 Physics of Inorganic Semiconductors

Understanding the fundamental physics of semiconductors provides the foundation for this study. To analyse temperature-dependent conductivity in organic semiconductors, we first review the physics of inorganic semiconductors, and then build upon that to explain conduction mechanisms in small molecule and polymer semiconductors.

2.2.1 Basic crystal structure

The fundamental electronic properties of semiconductors are closely linked to their crystalline structure. In crystalline semiconductors, their electrical properties are determined not only by their chemical composition but also by the precise arrangement of atoms within the crystal lattice. In a single-crystal material, there is regular geometric periodicity in the atomic arrangement. This periodicity creates a discrete, infinite and regularly repeating pattern of points in a vector space, which is called a lattice.

Figure 2.1 shows a two-dimensional array of lattice points. In this configuration, each dot represents a lattice site. A two-dimensional lattice is created by translating a lattice point along two non-collinear vectors, denoted as $\vec{a}_1$ and $\vec{a}_2$. These vectors define the periodicity and symmetry of the lattice in two dimensions.

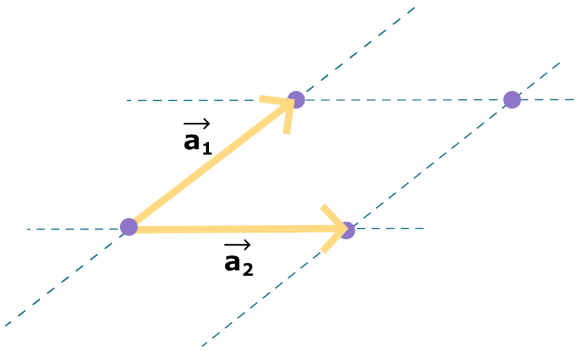

Figure 2.1: Two-dimensional view of a single-crystal lattice

By introducing a third non-coplanar translation vector, a complete three-dimensional lattice structure is formed, as illustrated in the figure below.

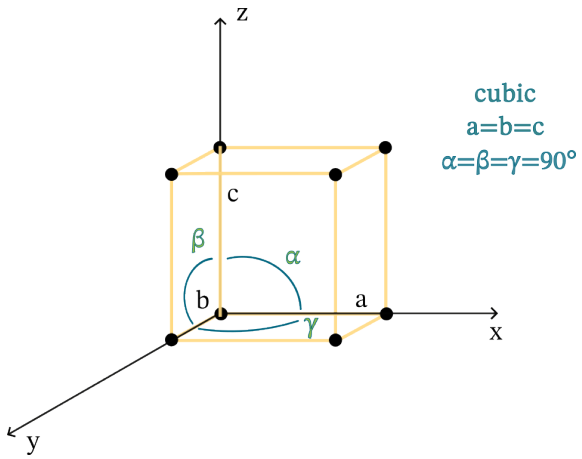

Figure 2.2: Three-dimensional single-crystal cubic lattice

To describe and analyse these periodic structures, it is useful to begin with the concept of the unit cell, which serves as a fundamental starting point. The unit cell is the smallest repeating unit that represents the full three-dimensional periodicity of the crystal. In three dimensions, it is defined as a parallelepiped whose vertices are lattice points. Mathematically, any lattice point can be expressed as:

$$\vec{R} = p\vec{a} + q\vec{b} + r\vec{c}, \quad p, q, r \in \mathbb{Z} \tag{2.1}$$

where $\vec{a}, \vec{b}, \vec{c}$ are the primitive vectors of the Bravais lattice, and $\vec{R}$ denotes the position of each lattice point. The integers p, q, and r specify how many steps one takes along each primitive vector direction, thereby mapping out all possible lattice points in space. A unit cell is illustrated in 2.3, showing how lattice points repeat in all spatial directions.

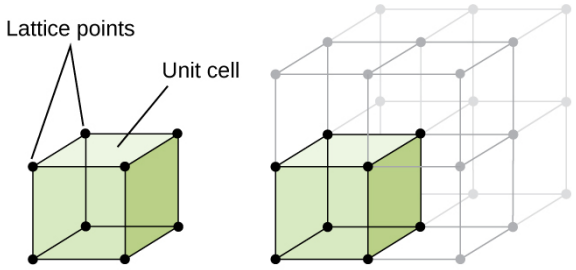

Figure 2.3: A unit cell shows the locations of lattice points repeating in all directions [32].

Silicon (Si) and germanium (Ge) are two widely used group IV semiconductors, both characterised by the diamond cubic structure, which is a specific type of crystal lattice. This arrangement arises from the electronic configuration of group IV elements, each possessing four valence electrons. To complete their outermost electron shells, each atom forms four covalent bonds by sharing its valence electrons with four nearest neighbours in the lattice. In this way, every atom is bonded to four adjacent atoms, forming a stable and repeating crystal structure. An illustration of the covalent bonding in silicon is shown below:

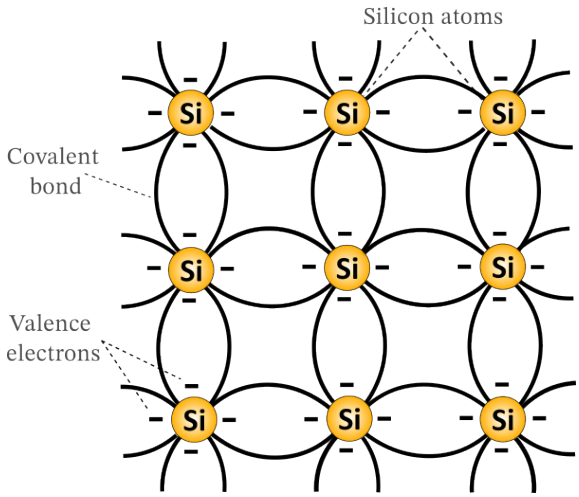

Figure 2.4: Representation of silicon valence electrons and covalent bonding in the silicon crystal. Adapted from [33].

In the diamond crystal structure, the spatial arrangement of atoms results in a tetrahedral geometry, with bond directions pointing toward the corners of a regular tetrahedron. The figure below also shows the unit cell of the diamond lattice, which represents the smallest repeating unit of the overall crystal structure.

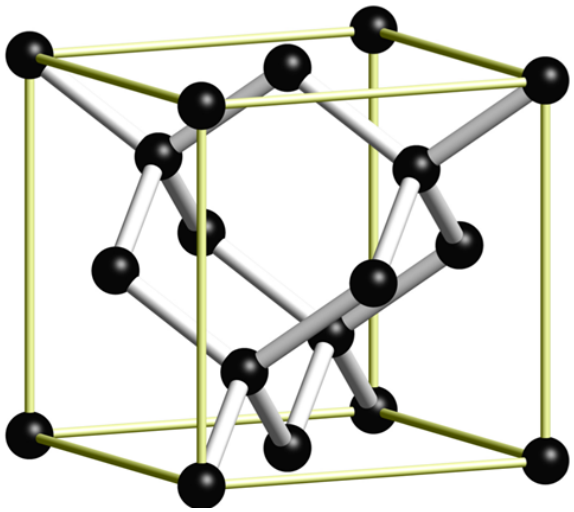

Figure 2.5: Unit cell of diamond lattice structure [34].

2.2.2 E-k relation

As shown in Figure 2.5, the diamond lattice presents a highly ordered and symmetric structure, which contributes significantly to the electronic properties of these materials. The strong covalent bonding and the spatial arrangement of atoms lead to a spatially periodic electrostatic potential field $V(\vec{r})$ that reflects the symmetry of the underlying lattice structure. This periodic potential satisfies the relation:

$$V(\vec{r} + \vec{R}) = V(\vec{r}) \tag{2.2}$$

where $\vec{R}$ is any lattice vector of the Bravais lattice.

Because the motion of electrons is governed by this periodic potential, their allowed quantum states differ fundamentally from those in isolated atoms. The Schrödinger equation shows that the energy of an electron is quantised, meaning each electron occupies a distinct orbital associated with a particular energy level rather than a continuous spectrum. In isolated atoms or small systems, these states are well separated; while in large crystals, the interactions among a vast number of atoms cause the discrete states to become very closely spaced. Once the separation between adjacent levels becomes much smaller than the thermal energy kT, they effectively merge into a quasi-continuum. This leads to the formation of energy bands and band gaps, concepts that will be elaborated upon later.

From the perspective of quantum mechanics, the state and dynamics of an electron are described by a wavefunction $\psi(\vec{r})$, governed by the time-independent

Schrödinger equation:

$$\left[-\frac{\hbar^2}{2m}\nabla^2 + V(\vec{r})\right]\psi(\vec{r}) = E\psi(\vec{r}) \tag{2.3}$$

where $\hbar$ is the reduced Planck constant, m is the effective mass of the electron, $V(\vec{r})$ is the potential energy experienced by the electron, and E is the corresponding energy eigenvalue.

When multiple atoms come close together to form a solid, their atomic orbitals overlap significantly. According to the Pauli exclusion principle, which states that no two fermions can have the same set of quantum numbers, the discrete energy levels of individual atoms split into a series of closely spaced states, thereby forming energy bands, as illustrated below.

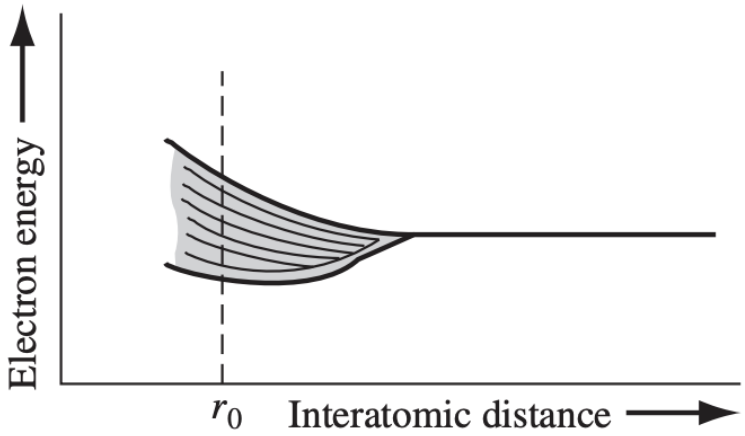

Figure 2.6: The splitting of an energy state into a band of allowed energies [35].

Within a crystal, the periodic potential of the lattice further organises these states into well-defined bands. The highest band that is fully occupied at absolute zero is the valence band (E_V), while the next higher-energy band that can accept additional electrons is the conduction band (E_C). The region between the top of

the valence band and the bottom of the conduction band, where no electronic states exist, is the band gap (E_g), which specifies the minimum excitation energy required for an electron to participate in conduction.

According to Bloch's theorem and the Schrödinger equation, the motion of an electron in such a periodic potential is described by a dispersion relation between its energy and wave vector, commonly referred to as the E-k relation:

$$E = E_n(\vec{k}) \tag{2.4}$$

This equation relates the electron's energy to the crystal wavevector $\vec{k}$ in the n-th band and characterises the band structure of a periodic potential.

To illustrate this relationship in practice, it is useful to consider the case of direct and indirect bandgap semiconductors. In a direct bandgap semiconductor such as GaAs, the conduction band minimum and the valence band maximum occur at the same point in k-space (typically at k =0). Near the band edges, the E–k relationship exhibits a symmetric parabolic shape, which reflects the effective mass of the charge carriers. Although the allowed electronic states are discrete in k-space, the E–k relationship can be depicted as a smooth and continuous curve, as illustrated below.

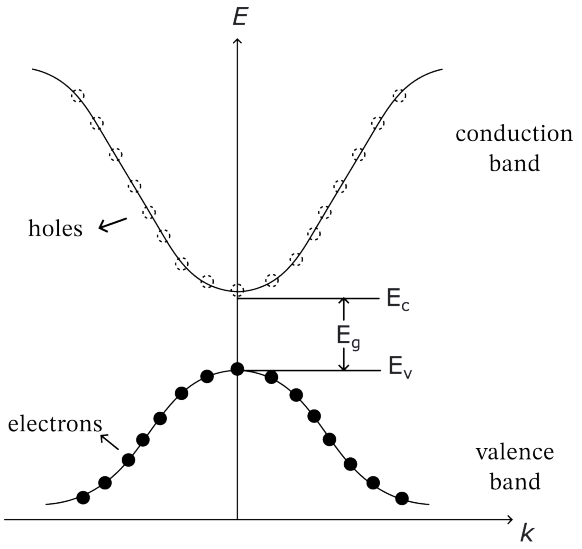

Figure 2.7: Schematic E-k band diagram for a direct bandgap semiconductor.

From the diagram, the E–k band structure reflects both the symmetry and the effective mass differences of carriers near the band edges. While electronic states are distributed across the entire band, it is only those near the band edges that govern electrical conduction, since carriers can be most easily excited there.

It should be emphasised that in the figure, the electrons (solid markers) and holes (open markers) are shown merely to indicate occupancy: they are immobilised in this static representation and therefore do not themselves contribute to conduction.

When an electron acquires sufficient energy, such as thermal energy or a photon hv, that is equal to or greater than the band gap, it can be excited from the valence band to the conduction band. As shown in the diagram below, shaded circles represent occupied states in k-space, while empty circles represent unoccupied states.

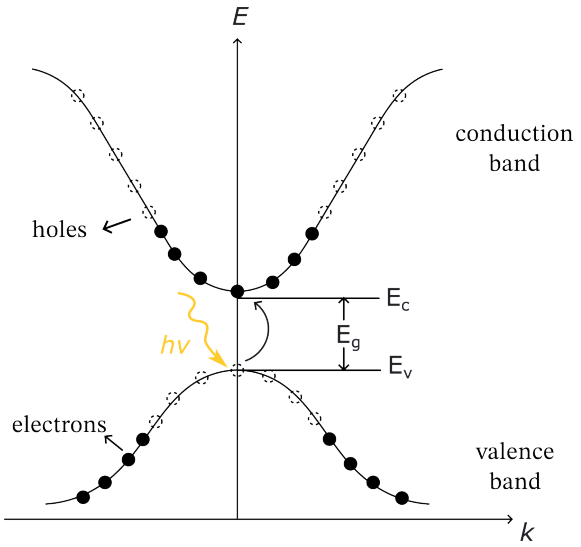

Figure 2.8: E-k diagram illustrating photon absorption in a direct bandgap semiconductor.

2.2.3 Band Theory

As illustrated in Figure 2.7, a band gap exists between the conduction band and the valence band. For an electron to transition from the valence band to the conduction band, it acquires sufficient energy to overcome this gap.

The band gap influences the electrical conductivity of materials, as a wide band gap requires a greater energy for electrons to transition between bands. For instance, insulators typically exhibit large band gaps (4–12 eV), meaning that very few electrons can reach the conduction band under normal conditions. Semiconductors have relatively smaller band gaps (typically 0.5–4 eV), allowing a considerable number of electrons to absorb thermal or optical energy from the environment and transition into the conduction band. In conductors, there is effectively no band gap. This arises in two ways: either the valence and conduction bands overlap in energy, or partially filled bands extend across the Fermi level. In both cases, electronic states are continuously available at the Fermi energy, so electrons do not require thermal

or optical excitation to become mobile. Consequently, even a small applied electric field can accelerate these electrons, leading to a high intrinsic electrical conductivity.

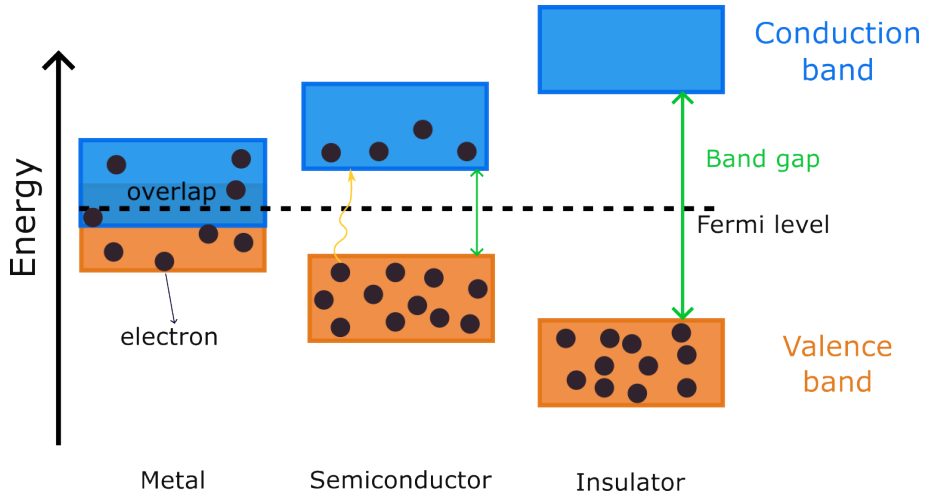

Figure 2.9: Schematic band gap diagrams for conductors, insulators, and semiconductors.

The band structure and band gap determine whether electronic transitions between energy bands are possible. To understand how electronic states are distributed within each band, particularly carrier concentration and transport behaviour, it is essential to consider the density of states (DOS).

2.2.4 Density of states

One critical factor influencing mobility is the density of states (DOS), which is typically characterised by a broad distribution of localised states, often modelled as exponential or Gaussian tails extending into the band gap. Deeper trap states, which are located farther from the transport levels, act as strong trapping centres from which carriers require significant thermal activation energy to escape. As a result, materials with a high density of deep trap states lead to reduced carrier mobility and enhanced recombination losses. Therefore, the shape and width of the DOS

distribution are key determinants of charge transport efficiency in organic electronic devices.

The DOS function represents the number of available quantum states per unit energy that can be occupied by electrons (or holes). It determines carrier concentrations and how carriers are distributed across energy levels. For a parabolic band structure in three dimensions, the density of states (DOS) in the conduction band is given by [36]

$$D_c(E) = \frac{1}{2\pi^2}\left(\frac{2m_e^*}{\hbar^2}\right)^{3/2}\sqrt{E - E_c}, \quad E \geq E_c \tag{2.5}$$

here, m_e^* is the effective mass of the electron, $\hbar$ is the reduced Planck constant, and E_c is the conduction band edge. The formula is valid for $E \geq E_c$.

2.2.5 Carrier Concentration and Fermi Level

In semiconductors, the total number of electrons is extremely large. For example, in a silicon crystal, the number of atoms is approximately 5×10^{22} atoms/cm^3, Since each silicon atom has four valence electrons, the corresponding electron density is about $4 \times 5 \times 10^{22}$ electrons/cm^3. At a given temperature, these electrons experience continuous random thermal motion. Electrons may absorb energy from lattice vibrations (phonons) to occupy higher-energy states, or release energy to phonons when relaxing to lower-energy states.

Although the energy of each electron constantly fluctuates, the entire electron population follows a well-defined statistical distribution at thermal equilibrium. Specifically, the probability that electrons occupy quantum states of various energies

is governed by a predictable statistical law. This probability function is known as the Fermi–Dirac distribution function, which describes the probability that a quantum state at a given energy is occupied by an electron:

$$f(E) = \frac{1}{1 + e^{(E-E_F)/kT}} \tag{2.6}$$

where $f(E)$ is the occupation probability of a state of energy E, E_F is the Fermi energy, k is Boltzmann's constant, and T is temperature in Kelvin.

At absolute zero, the Fermi level E_F marks the highest occupied electronic state. For metals, E_F lies within the conduction band and shifts negligibly with temperature.

In an intrinsic semiconductor, the Fermi level lies close to the middle of the band gap at $T = 0$, but at finite temperature, it can shift slightly depending on the effective masses and densities of states in the conduction and valence bands, that is

$$E_F \approx \frac{E_C + E_V}{2} \tag{2.7}$$

However, as we shall see in a following section of this chapter, the chemical potential in doped semiconductors has a significant temperature dependence.

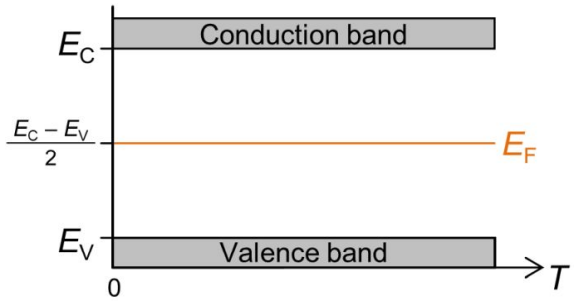

Figure 2.10: Fermi level in an intrinsic semiconductor [37].

An essential characteristic of semiconductors is that their electrical properties are strongly influenced by temperature. To illustrate this, we first consider intrinsic semiconductors, where the carrier concentration is determined solely by thermal excitation across the band gap.

In intrinsic semiconductors, the carrier concentration is strongly temperature dependent: At absolute zero, no free carriers exist, but with increasing temperature (above 0 K), thermal energy can excite electrons from the valence band into the conduction band, leaving behind holes in the valence band. This process is referred to as "intrinsic excitation", which generates electron–hole pairs, with equal concentrations of electrons and holes contributing to charge transport. The resulting temperature dependence of carrier density forms the basis for understanding semiconductor conductivity.

The intrinsic carrier concentration is given by

$$n_i = p_i \tag{2.8}$$

where n_i and p_i denote the intrinsic concentrations of electrons and holes, respectively. This relation indicates that, in thermal equilibrium, the electron and hole concentrations are equal in an intrinsic semiconductor.

The carrier concentrations are determined by the density of states and the Fermi–Dirac distribution. The electron concentration is given by

$$n = \int_{E_C}^{\infty} g_c(E)\, f(E, E_F, T)\, \mathrm{d}E \tag{2.9}$$

while the hole concentration is expressed as

$$p = \int_{-\infty}^{E_V} g_v(E)\ [1 - f(E, E_F, T)]\, \mathrm{d}E. \tag{2.10}$$

Here, n and p denote the electron and hole concentrations, respectively. $g_c(E)$ and $g_v(E)$ denote the density of states in the conduction and valence bands, respectively. E_C and E_V denote the conduction band minimum and valence band maximum, respectively, and $f(E, E_F, T)$ denotes the Fermi–Dirac distribution function.

2.2.6 Doping

At room temperature, only a small number of carriers are thermally excited in intrinsic semiconductors. For example, in silicon (Si) at 298 K, the intrinsic electron concentration is around 1.5×10^{10} cm^{-3}, whereas in gallium arsenide (GaAs) it is only 1.1×10^{6} cm^{-3} [38]. Such low carrier densities result in high electrical resistivity, limiting practical applications.

This limitation can be overcome through adding impurities (doping), which allows one to control the concentration of electrons and holes. By carefully doping donor- or acceptor-type dopants, additional electronic states are created within the band gap, thereby controlling the carrier concentration.

Taking silicon as an example, as a group IV element, each atom contributes four valence electrons. In pure silicon, the valence band is completely filled at absolute zero. When adding a very small number of atoms of a group V element, such as phosphorus (P), substituted into the lattice, each phosphorus atom has 5 valence

electrons, as shown in Figure 2.11.

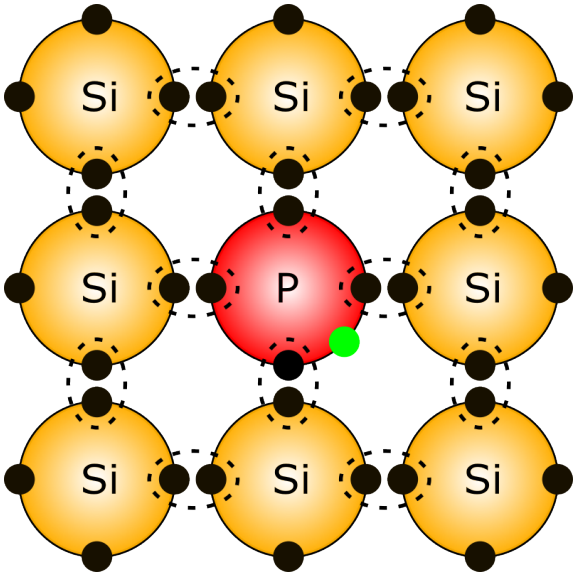

Figure 2.11: N-type semiconductor. The donor atom contributes one free electron, as shown in green. Adapetd from [39].

The fifth electron of phosphorus is weakly bound to the silicon lattice and can be ionised to become a conduction electron at a moderate temperature. The phosphorus atom is therefore referred to as a donor, and the silicon becomes n-type due to the introduction of additional negative charge carriers. This process creates discrete donor levels just below the conduction band, as illustrated in the schematic below. The ionised donor atoms are positively charged but remain immobile at fixed lattice sites, so the semiconductor as a whole remains electrically neutral, while the majority carriers in this case are electrons, as shown below.

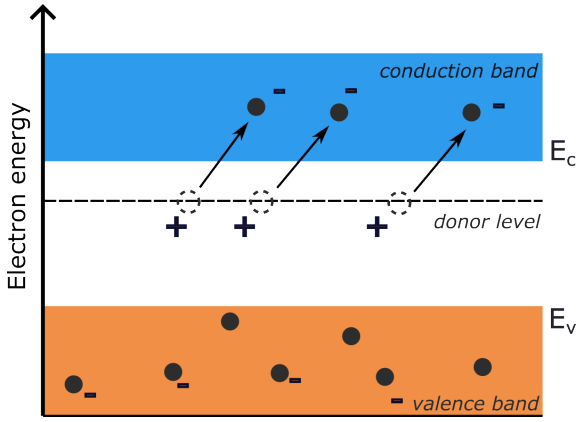

Figure 2.12: Schematic bond pictures for n-type Si with donor (with phosphorus). Adapted from [40].

Similarly, when adding a very small number of atoms of a group III element such as boron (B), they act as acceptors and introduce discrete energy levels slightly above the valence band edge. These acceptor levels can capture electrons from the valence band, thereby leaving behind holes.

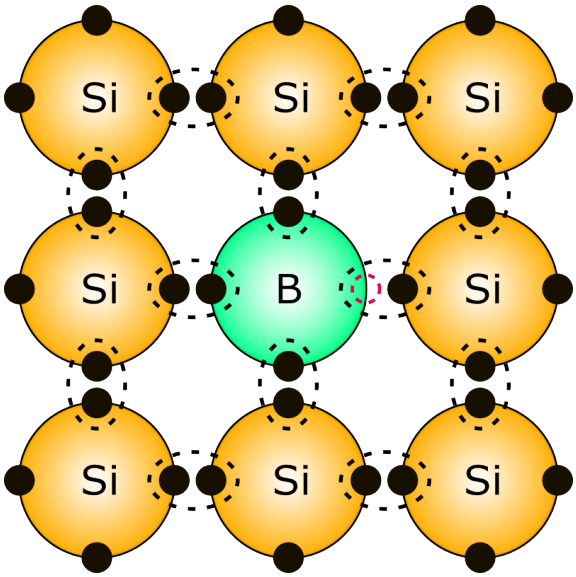

Figure 2.13: P-type semiconductor. The acceptor atom creates a hole, shown as a red circle. Adapetd from [39].

As a result, the majority carriers in this case are holes, and the material is referred to as a *p*-type semiconductor. The ionised acceptor atoms are negatively

charged but remain immobile at fixed lattice sites, so the semiconductor as a whole remains electrically neutral, while the majority carriers in this case are holes, as illustrated below

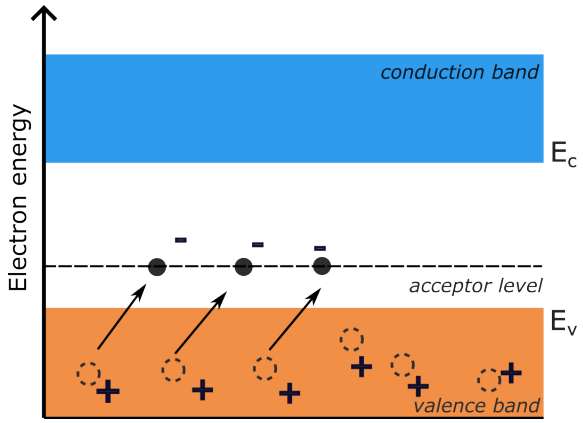

Figure 2.14: Schematic bond pictures for (a) n-type Si with p-type Si with acceptor (boron). Adapted from [40].

2.2.7 Carrier Transport Phenomena

Carrier Drift

When an external electric field is applied to a semiconductor, it exerts a force on the charge carriers (both electrons and holes), causing them to move with a net, non-zero average velocity. This directed transport of carriers under the electric field is known as drift. The resulting drift current densities are given by

$$J_n = qn\mu_n E, \quad J_p = qp\mu_p E \tag{2.11}$$

where J_n and J_p are the electron and hole current densities, q is the elementary charge, n and p are the electron and hole concentrations, μ_n and μ_p are their respective mobilities, and E is the applied electric field.

The parameter μ, known as the carrier mobility, characterises how easily charge

carriers move in response to an applied electric field. It is defined as the ratio of the drift velocity v_d to the electric field E:

$$\mu = \frac{v_d}{E}. \tag{2.12}$$

Although carriers are accelerated by the electric field, their motion is constantly interrupted by scattering with phonons, impurities, and lattice imperfections. As a result, carriers do not accelerate indefinitely but quickly reach a steady-state average drift velocity that is proportional to the applied field. This steady-state behaviour is quantified by the mobility.

According to this concept, the electrical conductivity σ of a semiconductor can be expressed as

$$\sigma = q(n\mu_n + p\mu_p) \tag{2.13}$$

where q is the elementary charge, n and p are the electron and hole concentrations, and μ_n and μ_p are the electron and hole mobilities.

Thus, the conductivity is directly proportional to both the carrier concentration and the mobility, highlighting the dual importance of carrier density and scattering mechanisms in determining the transport properties of semiconductors. While the above discussion focuses on drift, the total current in a semiconductor also includes a diffusion component, which will be discussed in the following section.

Carrier Diffusion

Another fundamental transport mechanism is diffusion, which arises from the non-uniform spatial distribution of charge carriers. A concentration gradient drives

carriers from regions of higher concentration to regions of lower concentration, which tends to restore thermodynamic equilibrium.

Electrons diffuse in the direction of decreasing electron concentration, while holes move in the direction of decreasing hole concentration. Since electrons and holes carry opposite charges, their diffusion leads to currents in opposite directions.

2.3 Organic Semiconductors

Organic semiconductors differ fundamentally from the conventional inorganic semiconductors discussed earlier, such as silicon-based materials. In this section, we take a closer look at the materials that conform organic sensors. Organic polymers and organic molecules constitute the active semiconducting layers in organic sensors [19]. Generally speaking, "organic" materials are defined as carbon-based compounds, primarily composed of carbon and hydrogen, often with a few heteroatoms.

Although most carbon-based polymers are electrically insulating in their pristine form, such as conventional plastics, they can be engineered to exhibit semiconducting or even highly conductive behaviour. In particular, introducing extended π-conjugation along the polymer backbone enables charge delocalisation. Charge transport in these materials is typically governed by thermally activated hopping between localised states, especially in disordered thin films, rather than band-like transport as observed in crystalline inorganic semiconductors [41].

In 1974, polyacetylene (PA) was first synthesised using a Ziegler–Natta catalyst [42], marking the beginning of organic electronics. Three years later, Heeger

et al. demonstrated that iodine-doped trans-polyacetylene reached conductivities of 10^5 S/m, the highest reported for a polymer at the time [43]. This breakthrough proved that doping π-conjugated polymers could yield metallic-like conductivity and laid the foundation for the development of conducting polymers. Subsequent advances in molecular engineering, particularly through donor–acceptor (D–A) polymer architectures, enabled systematic tuning of energy levels and bandgaps to optimise charge transport [44, 45].

Beyond molecular design, microstructural organisation plays a critical role in determining electrical performance. It has been shown that aggregation, molecular ordering and energetic disorder strongly influence carrier mobility in conjugated polymers [46]. As a result, processing conditions such as solution concentration and film thickness can significantly affect the electrical behaviour of solution-processed devices.

Today, organic semiconductors are widely employed in flexible and lightweight electronic systems, including transistors, light-emitting diodes and sensors [47, 48]. Their mechanical flexibility and solution processability make them particularly attractive for wearable and temperature-sensitive applications.

2.3.1 Working principle of Organic Semiconductors

Typically, organic semiconductors are grouped into small molecules and polymers. The former is normally referred to as oligomers, containing a few mers or repeat units per molecule, whereas the polymers comprise numerous repeat units. In both types, the electronic properties are primarily determined by carbon-based

bonding frameworks and orbital hybridisation. As discussed previously, the spatial distribution of these electrons can be described by atomic orbitals, which are solutions to the Schrödinger equation for a single atom. While many types of orbitals exist, in the context of organic semiconductors, the most relevant are the s and p orbitals, since the valence electrons of carbon and silicon primarily occupy these states and thereby determine bonding and electronic behaviour. For this reason, the following discussion focuses on the s and p orbitals and their hybridisations.

The s orbital is spherically symmetric around the atomic nucleus, with electron density uniformly distributed in all directions. The p orbitals exhibit a dumbbell-shaped electron density distribution oriented along one of the three Cartesian axes (x, y, or z). Each orbital is labelled with a principal quantum number, which indicates its energy level. The spatial distribution of atomic orbitals is illustrated in Figure 2.15, which shows the shapes and orientations of the 2s and 2p orbitals.

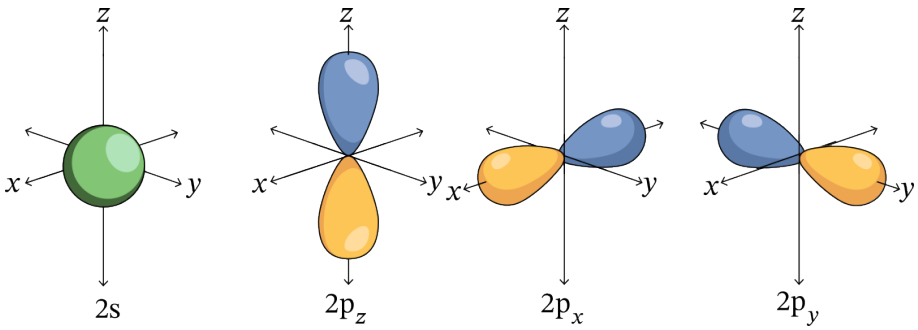

Figure 2.15: Schematic representation of s orbital and p orbitals. Adapted from [49].

When s and p orbitals merge, they form linear combinations that give rise to new hybrid orbitals. This hybridisation may involve all or part of the orbitals. For example, a carbon atom with the electronic configuration of $1s^2 2s^2 2p^2$, which represents 2 electrons in the 1s orbital, 2 electrons in the 2s orbitals, and 2 electrons in the 2p orbitals. To form equivalent bonds, the 2s and 2p orbitals cannot be used

independently; instead, they hybridise to generate new orbitals with the required symmetry.

When hybridisation involves all four orbitals (one 2s and three 2p orbitals), four equivalent sp^3 hybrid orbitals are produced, each oriented tetrahedrally. If the hybridisation involves 2s orbital and two 2p orbitals (e.g., $2p_x$ and $2p_y$ orbitals), three sp^2 hybrid orbitals are generated, lying in a trigonal planar geometry with inter-orbital angles of 120°. If hybridisation occurs only between the 2s orbital and only one 2p orbital, two linearly oriented sp orbitals are produced, separated by a bond angle of 180°.

In the case of sp^2 hybridisation, one *s* orbital (red) combines with two p orbitals (blue) to form three equivalent sp^2 hybrid orbitals (orange). These hybrid orbitals adopt a trigonal planar geometry with inter-orbital angles of 120°. The remaining unhybridised p orbital is oriented perpendicular to this plane (along the z axis) and can participate in π bonding, which will be discussed later.

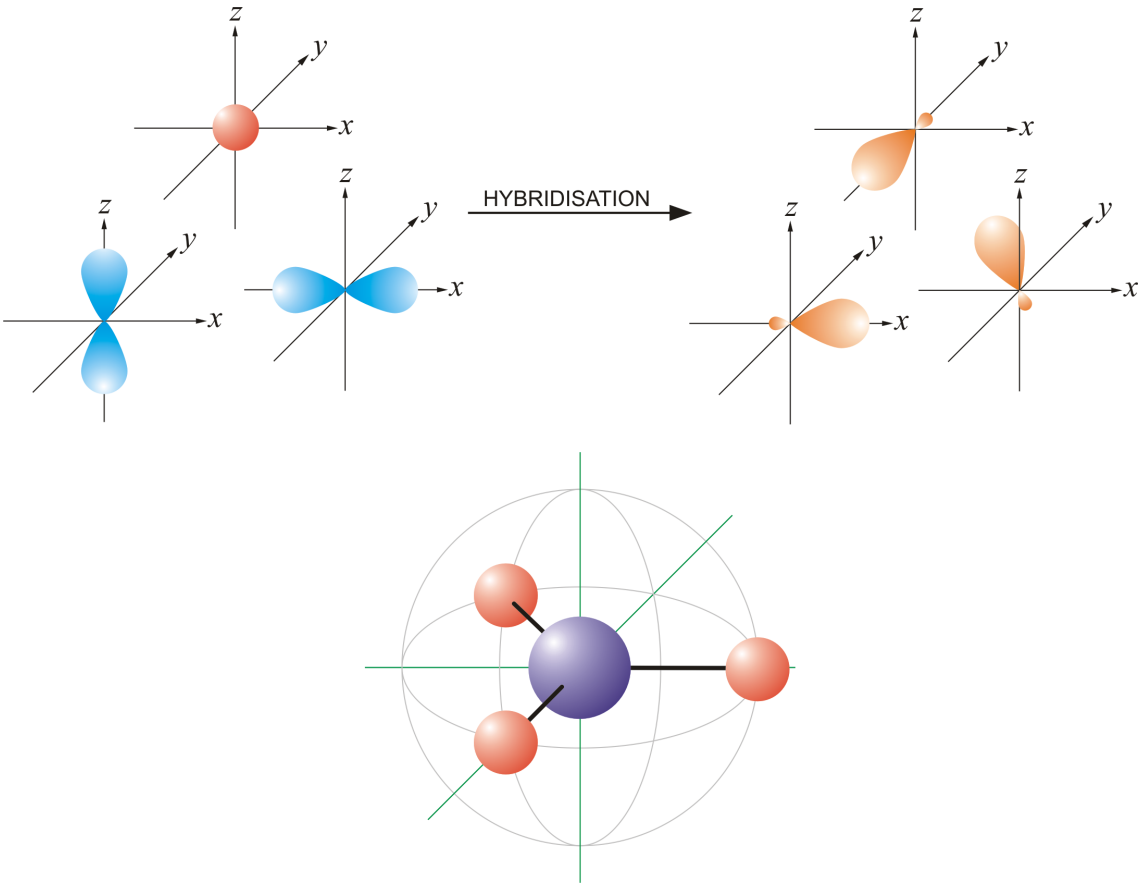

Figure 2.16: An sp^2 hybrid orbital is formed by the linear combination of one s and two p orbitals of comparable energy (such as 2s and 2p orbitals) on the same atom. The three sp^2 hybrid orbitals lie in a plane with an inter-orbital angle of 120°. The remaining p orbital remains unhybridised and is perpendicular to the plane of the three sp^2 orbitals [50].

In organic molecules, when two atomic orbitals overlap, they combine to form molecular orbitals. The fundamental types of bonds are σ and π bonds. The number of hybrid orbitals and the remaining unhybridised p orbitals determine the number and type of chemical bonds that can form. Taking Ethylene (C_2H_4) as an example, each carbon atom has four valence electrons, three of these electrons form sp^2 hybrid orbitals, which form σ bonds with two hydrogen atoms and the other carbon atom. The remaining valence electron occupies an unhybridised $2p_z$ orbital, which is perpendicular to the plane created by the three σ bonds. The $2p_z$ orbitals

on each carbon atom overlap side-by-side to form a π bond, with electron density distributed above and below the molecular plane. Unlike the highly localised electron density between nuclei in a σ bond, the electron density in a π bond is delocalised, contributing significantly to the planarity and rigidity of the ethene molecule, as illustrated below.

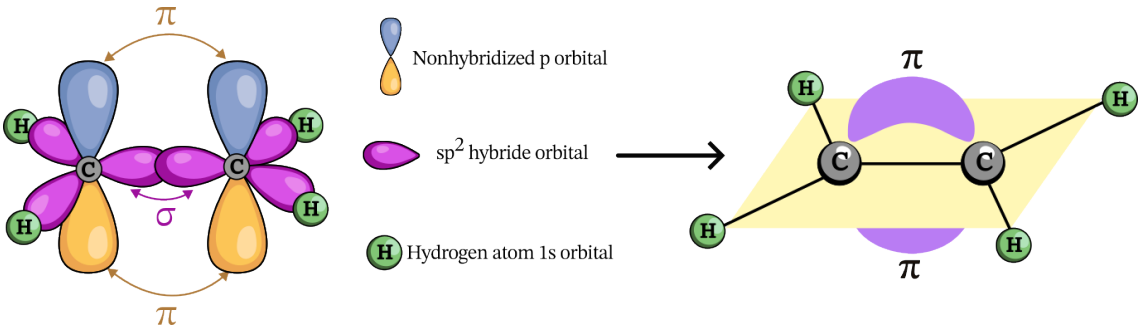

Figure 2.17: Schematic illustration of sp^2 hybridization and π bond formation. Adapted from [49].

According to the principle of quantum mechanics, when atomic orbitals combine, they form bonding and anti-bonding molecular orbitals. In discrete molecules, the highest occupied molecular orbital (HOMO) and the lowest unoccupied molecular orbital (LUMO) define the energy window relevant for charge transport. A more detailed understanding of how these bonding interactions contribute to energy level formation and electronic band structures is explained in Figure 2.18.

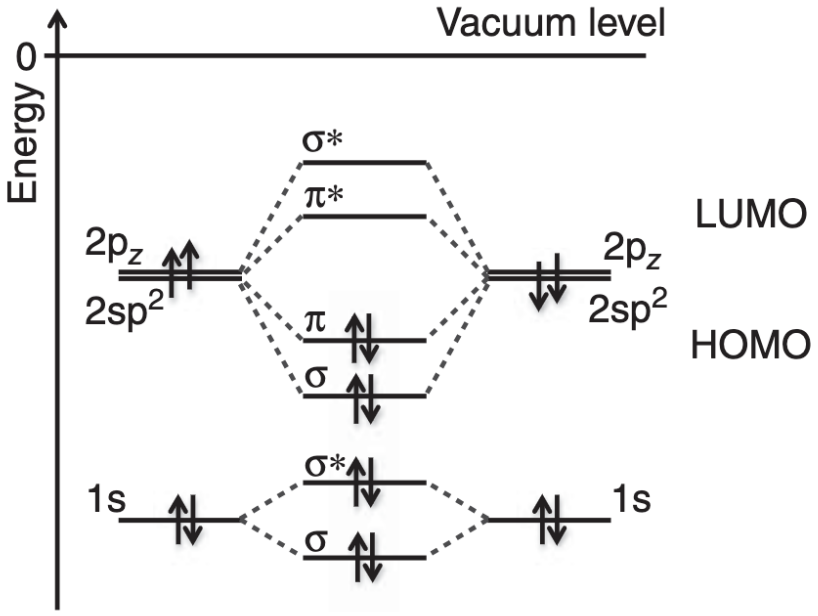

Figure 2.18: Simple energy level diagram illustrating the formation of σ and π bonds from atomic orbitals for ethene. As the length of the conjugated system increases, the energy levels become more closely spaced, and the bandgap decreases. Only orbitals involved in the carbon-carbon interaction are shown. The two $2sp^2$ hybrid orbitals forming σ-bonds with hydrogen atoms are omitted [51].

In σ-bonded systems, the electrons are strongly confined between the bonded nuclei, which results in a wide band gap and poor conductivity. By contrast, π-bonded electrons, formed through the lateral overlap of adjacent p_z orbitals, are distributed above and below the molecular plane. When multiple atoms are connected through consecutive π bonds, orbital interactions lead to extended delocalisation across the backbone, which is a phenomenon known as π-conjugation. This delocalisation reduces the band gap and enhances charge transport.

In extended π-conjugated systems such as polymers and molecular crystals, intermolecular orbital overlap leads to the formation of energy bands. As the number of atoms (or π electrons) in the conjugated system increases, electron delocalisation is further enhanced, causing the HOMO–LUMO gap to narrow further. The extent

of this orbital overlap directly influences the bandgap, therefore determining the electronic properties of the material.

Experimental evidence and theoretical studies have demonstrated that π-electron delocalisation (through π–π overlap) significantly improves charge generation and mobility. Such π electron delocalisation effects are particularly pronounced in molecules incorporating benzene rings. Benzene rings are highly stable units with fully delocalised π-electrons over a planar six-membered ring and serve as fundamental structural motifs in many conjugated molecules. High-performance small-molecule semiconductors based on benzene-derived cores often present crystallised structures with efficient π–π stacking, supporting band-like transport mobilities on the order of 1 to 10 $\times 10^{-3}$ $\mathrm{cm}^2/\mathrm{V} \cdot \mathrm{s}$ at room temperature [52].

Unlike inorganic semiconductors, which contain intrinsic free charge carriers (electrons and holes) thermally excited across the band gap, organic semiconductors typically lack free carriers at room temperature. Instead, charge transport occurs through quasi-particles known as polarons, which are coupled with local lattice or molecular backbone distortions. In terms of polymeric organic semiconductors, extended delocalisation of π bonds along the carbon backbone can generate quasi-one-dimensional electronic systems. However, because of structural and energetic disorder inherent in real organic systems, the energy level distribution is not ideal.

To discuss the energetic disorder in organic systems, the density of states (DOS) is often modelled using phenomenological functions, most commonly Gaussian distributions [53, 54]. Up to now, there has been no direct experimental evidence verifying specific DOS models. Thus, the DOS is typically estimated by comparing

experimental data with theoretical models using trial DOS functions.

Within the Gaussian DOS framework, energetic disorder is primarily represented by the widths σ_L and σ_H, which arise from local electrostatic environments. By contrast, variations in conjugation length predominantly affect the band gap E_g rather than the DOS shape, as discussed below.

$$\begin{aligned} g_L(E) &= \frac{N_0}{\sqrt{2\pi}\sigma_L} \exp\left[-\frac{(E-E_L)^2}{2\sigma_L^2}\right], \\ g_H(E) &= \frac{N_0}{\sqrt{2\pi}\sigma_H} \exp\left[-\frac{(E-E_H)^2}{2\sigma_H^2}\right], \end{aligned} \tag{2.14}$$

where N_0 is the total number of states per unit volume, which in organic molecular materials can be approximated by the molecular number density (i.e. the number of molecules per unit volume). E_L and E_H represent the average energies of the LUMO and HOMO levels, while σ_L and σ_H represent their respective energetic disorder (distribution widths). Typical values of σ in organic semiconductors range from 0.05 to 0.20 eV [53].

These models assume that all states in disordered organic semiconductors are localised [55]. In this situation, the Gaussian distributions of the HOMO and LUMO states lead to significant tailing into the nominal bandgap, resulting in a non-zero DOS in this energy range. However, in more ordered systems, states closer to the centre of the DOS distribution may exhibit partial delocalisation and contribute to band-like transport. Thus, a mobility edge is often assumed to exist, separating the extended states near the DOS peak from the localised tail states. To reconcile these regimes, the concept of a mobility edge is introduced, separating extended states near the DOS peak from localised tail states [53].

Under external excitation (thermal or optical), electrons can be promoted from the HOMO to the LUMO, altering the molecule's electronic properties. A simple particle-in-a-box model qualitatively describes this behaviour, showing that the band gap E_g is inversely proportional to the conjugation length N:

$$E_g = \frac{(N+1)^2\pi^2\hbar^2}{2m(Na)^2} - \frac{N^2\pi^2\hbar^2}{2m(Na)^2} \approx \frac{\pi^2\hbar^2}{2mNa^2} \tag{2.15}$$

where N is the number of atoms (or repeating units) in the conjugated chain, a is the spacing between atoms, Na represents the effective length of the conjugated π system, m is the effective mass of an electron, and $\hbar$ is the reduced Planck constant.

The formula shows that band gap E_g is inversely proportional to the chain length N, leading to stronger delocalisation and, in the limit of $N \to \infty$, metallic behaviour.

Thus, the particle-in-a-box approximation provides a qualitative explanation for the correlation between conjugation length and bandgap in organic semiconductors, emphasising that extended π-systems favour narrower gaps and enhanced delocalisation.

2.3.2 Organic semiconductors Doping

A desirable way to obtain charged organic materials is to introduce dopants that can act as electron donors through redox reactions to modulate carrier concentration. Common doping approaches include:

P-type doping (oxidation reaction): electrons are removed from the organic semiconductor by strong electron acceptors such as I_2, $FeCl_3$, and F_4TCNQ [56, 57]. For example:

$$[\mathrm{CH}]_n + 3\,\mathrm{I_2} \longrightarrow [\mathrm{CH}]_n{}^{2+} + 2\,\mathrm{I_3}^- \tag{2.16}$$

This reaction represents oxidative doping, where iodine (I_2) acts as an oxidising agent. The polymer loses electrons and becomes positively charged ($[CH]_n{}^{2+}$), while iodine is reduced to triiodide ions ($I_3{}^-$). This process increases hole concentration, making the material p-type.

N-type doping (reduction reaction): Electrons are donated to the material by strong electron donors such as Na, Cs, benzimidazoline radicals, and n-DMBI [58,59]. For example:

$$[\mathrm{CH}]_n + \mathrm{Na} \longrightarrow [\mathrm{CH}]_n{}^- + \mathrm{Na}^+ \tag{2.17}$$

In reductive doping, sodium (Na) donates an electron to the polymer, generating negatively charged species ($[CH]_n{}^-$). This increases the number of free electrons and leads to n-type conduction.

These reactions are classified as chemical doping, one of the most widely adopted doping strategies in organic semiconductors. In [60], organic salts have been successfully employed for n-type doping. This paper used cationic dyes, which are positively charged organic molecules, combined with suitable counterions to enable charge transfer in materials with low-lying LUMO levels (i.e. high electron affinity), such as electron-transport layers in organic photovoltaic devices. In such systems, ionic species modulate the charge-carrier density through electrostatic interactions.

Another widely explored method is precursor doping, which involves latent dopants that release charge carriers (electrons or holes) upon thermal activation or process-

ing. In [61], this method improves doping stability by preventing dopant diffusion and degradation. A representative example is n-DMBI-H, a thermally activated n-type dopant widely used in organic electronics. Upon thermal activation, it undergoes a hydride transfer reaction that donates electrons to the host semiconductor, thereby increasing carrier density. Its high efficiency, thermal stability, and broad compatibility with organic materials have established n-DMBI-H as a benchmark dopant for achieving reliable n-type conduction [62].

2.3.3 Charge Transport in Organic Semiconductors

Organic semiconductors do not follow a single universal charge transport model. Instead, several mechanisms have been proposed depending on the degree of molecular order and the specific experimental conditions, including band-like transport, multiple trapping and release, and hopping [63]. In highly ordered systems, such as single crystals or conjugated polymers with minimal torsional disorder, typically present band-like transport [64]. In these materials, molecules are bound only by relatively weak van der Waals forces, which results in narrow conduction and valence bands, usually a few hundred millielectronvolts in width. At low temperatures, electrons can still propagate within these bands as Bloch waves, similar to charge transport in inorganic semiconductors.

By contrast, in molecular crystals, the effective mass of charge carriers is significantly larger, and their mobility is lower, primarily because of the intrinsically narrow bandwidth. When the carrier mean free path becomes comparable to the lattice constant, the conventional band-like transport model no longer applies. In

this regime, the hopping mechanism provides a more appropriate description, where electrons or holes are thermally activated to jump between localised molecular orbitals.

In conducting polymers, the carrier density remains nearly constant since the dominant carriers (solitons, polarons, and bipolarons) already exist in the material [65]. Solitons are topological excitations that arise in polymers with degenerate ground states, polarons are charge carriers that become self-localised due to coupling with local distortions in the molecular backbone, and bipolarons are doubly charged species formed by the pairing of two polarons, often stabilised in heavily doped systems. Carriers transport via thermally assisted hopping or quantum tunnelling between localised states, particularly in amorphous or highly disordered organic semiconductors. To describe this behaviour, theoretical descriptions often use percolation theory [66], Bässler's Gaussian Disorder Model (GDM) [67] and the variable range-hopping mechanism [68].

Charge transport in polycrystalline or partially ordered organic semiconductors is often described by the mobility-edge model [69], which shares conceptual similarities with the multiple trapping and release (MTR) model. In this model, carriers occupying extended states above a critical energy (the mobility edge) contribute to band-like conduction, while those below it are localised and require thermally activated hopping. This model is particularly applicable to polycrystalline organic semiconductors with relatively low degrees of structural disorder.

Overall, efficient charge transport requires that charge carriers can move between molecules without being trapped or scattered. The carrier mobility is influenced by

a range of factors, including molecular packing, structural disorder, the presence of impurities, temperature, electric field, carrier density, molecular size or weight, and external pressure [67]. The following sections will focus on selected examples illustrating these effects.

Disorder

In disordered organic semiconductors, charge transport is strongly influenced by both electronic localisation and polaronic effects, where carriers couple to local lattice distortions and form self-localised quasi-particles [67]. Organic polymers are inherently disordered materials, consisting of chains with various lengths and non-uniformly distributed defects within the chain. Thus, they exhibit a distribution of conjugation lengths, defined as the effective distance over which electrons are delocalised along the chains. The bulk materials typically contain crystalline domains, whose size can reach tens of nm and amorphous domains, as illustrated in the figure below. In such disordered materials, charge transport is fast along the chains, moderate between the chains, and slow between the lamellar planes, which are the layered stacking motifs formed by polymer backbones and side chains [70]. Moreover, polymer chains may be randomly oriented in the x, y, or z axes. As illustrated in Figure 2.19, transport is expected to be more efficient in the ordered configuration 2.19(a) rather than in the disordered one Figure 2.19(c). It is widely accepted that high carrier mobility is linked to the degree of order and the stacking between the chains. Both high carrier mobility and efficient intra- and inter-chain transport are therefore essential to optimise the transport properties of conducting polymers.

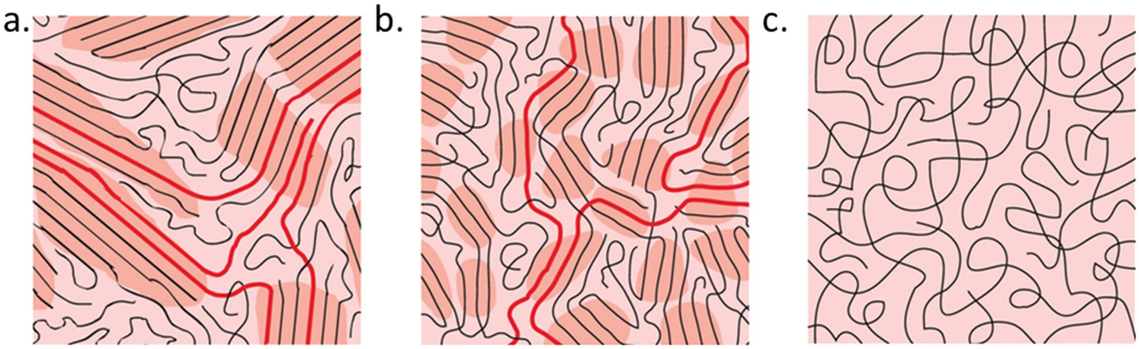

Figure 2.19: Schematic structure of polymers with different disorder levels [71](a) Very ordered, (b) disordered aggregates and (c) completely disordered. Depending on the density of the polymer, long chains (highlighted in red) can connect ordered regions (darker orange ones) without significant loss of the conjugation length.

Temperature

Single crystals and disordered organic materials exhibit distinct temperature dependencies of charge carrier mobility. In single crystals, both hole and electron mobilities typically increase as the temperature decreases. In contrast, disordered organic materials rely on thermally activated hopping between localised states, so their mobility generally rises with increasing temperature.

One of the earliest and most widely applied models to describe this mechanism is Mott's variable-range hopping (VRH) theory [72]. In this model, the hopping probability depends on both the spatial separation and the energy difference between localised sites. For temperatures between 10 – 300 K, transport is typically dominated by this VRH model. As the temperature increases, thermal energy enhances the charge carriers' hopping rate and overall carrier mobility. This behaviour is commonly described as [73]:

$$\rho = \rho_0 \exp\left(\left(\frac{T_0}{T}\right)^{\frac{1}{1+D}}\right) \tag{2.18}$$

where ρ is the resistivity, ρ_0 the prefactor at infinite temperature, T the absolute temperature, T_0 the characteristic temperature, and D the system dimensionality.

When temperatures exceed 300 K, the charge transport mechanism shifts to nearest-neighbour hopping (NNH), where charge carriers predominantly hop to the closest localised sites. The transport behaviour can be described by the Arrhenius equation [74, 75]:

$$\rho(T) = \rho_0 \exp\left(\frac{E_a}{kT}\right) \tag{2.19}$$

where ρ_0 is the pre-exponential factor, E_a the activation energy, and k the Boltzmann constant. In this regime, the hopping distance is short and relatively uniform, so thermal activation governs charge transport, and the mobility (or equivalently the resistivity) follows an Arrhenius-type temperature dependence.

2.3.4 PCDTPT Properties and Device Applications

Conjugated polymers consist of alternating single and double bonds along their backbone, enabling the delocalisation of π-electrons and resulting in semiconducting behaviour [44, 76]. Among various conjugated polymer systems, donor–acceptor (D–A) polymers represent one of the most successful molecular design strategies for bandgap engineering [77]. By alternating electron-rich donor units with electron-deficient acceptor units along the backbone, intramolecular charge transfer is enhanced, resulting in reduced bandgaps, tunable HOMO/LUMO energy levels, and improved intermolecular interactions [78]. In such systems, the HOMO is typically localised on the donor moiety and the LUMO on the acceptor moiety, enabling

rational control of electronic structure through chemical design [79, 80].

Among D–A polymers, PCDTPT [poly[(4,4-bis(2-ethylhexyl)cyclopenta[2,1-b:3,4-b′]dithiophene)-2,6-diyl-alt-[1,2,5]thiadiazolo[3,4-c]pyridine]] has attracted considerable attention for its narrow bandgap, high intrinsic mobility, and favourable molecular packing characteristics [81]. As a representative D–A copolymer, it consists of cyclopentadithiophene (CDT) donor units and pyridyl-thiadiazole (PT) acceptor units arranged in a regioregular backbone [81], as illustrated in Fig. 2.20.

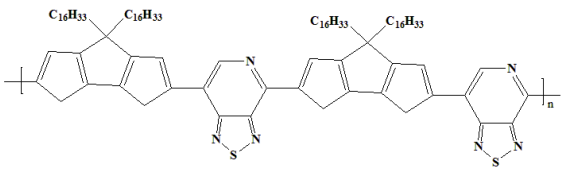

Figure 2.20: Chemical structure of PCDTPT

PCDTPT features a relatively shallow HOMO level of −5.14 eV [82] and a largely planar backbone, which together promote strong π–π stacking and efficient intermolecular charge transport [83]. The long alkyl side chains further improve solubility and facilitate the formation of uniform thin films through solution-processing techniques such as spin coating [84]. The charge transport performance of PCDTPT is highly sensitive to film morphology and processing conditions. Beyond its intrinsic molecular properties, structural studies have shown that molecular packing and domain ordering play a critical role in defining charge transport pathways, highlighting the importance of processing-induced morphology control [81]. Bottom-gate/top-contact PCDTPT field-effect transistors fabricated on octyltrichlorosilane (OTS)-treated SiO_2 typically exhibit hole mobilities of around 0.6 $cm^2\ V^{-1}\ s^{-1}$ [85].

By inducing macroscopic molecular alignment, significantly higher mobilities of up to 23.7 cm^2 V^{-1} s^{-1} have been achieved in PCDTPT films on nano-grooved SiO_2 substrates [83]. Interface engineering strategies, such as incorporating a graphene interlayer, have also been shown to enhance mobility to 13.08 cm^2 V^{-1} s^{-1} [86].

PCDTPT has attracted interest for organic thermoelectric applications. In PCDTPT thin films, the combination of narrow bandgap character, high intrinsic mobility and strong intermolecular interactions enables measurable and reproducible resistance variations with temperature [82]. These characteristics make PCDTPT a suitable candidate for flexible, solution-processed temperature sensing platforms, particularly in applications where mechanical compliance and low-temperature fabrication are required. Suh et al. demonstrated that chemically doped PCDTPT exhibits significantly enhanced electrical conductivity together with a measurable Seebeck coefficient, highlighting its intrinsically high carrier mobility and tunable transport characteristics [82]. This study reported a clear temperature dependence of electrical conductivity, which supports the suitability of PCDTPT for resistive-type temperature sensing applications. In addition to chemical doping, interface engineering has also been explored as an effective strategy to further optimise thermoelectric performance. Surface modification using self-assembled monolayers (SAMs) has been shown to enhance the thermoelectric performance of SWCNT-based organic composites [87]. In this system, PCDTPT interacts with SWCNTs through π-π interactions, which helps to modulate the carrier concentration and improve the Seebeck coefficient without significantly reducing electrical conductivity. The device achieves a maximum output power of 2.36 μW at $\Delta T = 50$ K, two times higher than

the unmodified substrate.

The photo-sensing ability of PCDTPT has also been explored. Wu et al. [88] demonstrated multilevel optical memory devices employing CdSe/ZnS quantum dots blended with poly(methyl methacrylate) (PMMA) as the floating gate layer in both vertical and planar configurations. The vertical devices exhibit a high photoresponsivity of 104 A W^{-1} and a photosensitivity of 200, significantly outperforming their planar counterparts. In addition to device architecture optimisation, material engineering strategies have also been explored to enhance photoresponse. The incorporation of [6,6]-phenyl C_{61}-butyric acid methyl ester (PCBM) to form a bulk heterojunction (BHJ) with PCDTPT has been shown to improve the photoresponsivity in both planar and vertical configurations [89]. Beyond conventional device geometries, PCDTPT has also been explored in ion-gated transistor architectures. The formation of an electric double layer enables high interfacial capacitance and efficient carrier modulation at voltages below 1 V. These devices exhibit mobilities of 1 cm^2 V^{-1} s^{-1} and good mechanical flexibility. Ion-gating also enables functionalities such as photoresponse, highlighting the potential of PCDTPT for low-power sensing and flexible electronics [90].

In organic photovoltaic (OPV) applications, early studies demonstrated that incorporation of PCDTPT and phenanthro[9,10-c][1,2,5]thiadiazole-based acceptor unit enables relatively high open-circuit voltages of up to 0.9 V in OPV devices [91]. More recent studies have focused on improving OPV performance through structural optimisation. In [92], the role of fibrillar morphology in governing charge transport was investigated, where the formation of semi-ordered fibrillar networks was shown

to provide efficient carrier transport pathways.

PCDTPT has also been employed in polymer-based light-emitting field-effect transistors (LEFETs), where it works as a high-mobility charge transport layer, enabling efficient hole injection and transport. Mobilities of around 2.1 cm^2 V^{-1} s^{-1} have been reported, along with an external quantum efficiency of 1.6% at a luminance of 2600 cd m^{-2}, as well as large-area emission [93].

PCDTPT has also been explored as a gas-sensing material in FET-based devices. Ultrathin (<10 nm) nanoporous films prepared via a phase inversion process exhibit significantly enhanced sensitivity, due to increased surface area, improved gas diffusion, and efficient charge transport [94]. The pore morphology can be tuned by controlling the immersion time, with an optimal duration of around 3s yielding the best sensing performance. These devices demonstrate an ultrahigh response of 2.46×10^6%, a low limit of detection below 1 ppm, and excellent selectivity towards NO_2 over other gases(6 ppm NO_2, 50 ppm H_2S, 50 ppm SO_2, 50 ppm NH_3, and 30 ppm CO). Recent research has demonstrated the feasibility of mechanically robust OFET-based gas sensors. Tang's group reported stretchable gas sensors based on polymer semiconductors with PCDTPT [95]. These devices can sustain strains of up to 100% while maintaining stable transfer characteristics, with negligible variation in on/off current and charge carrier mobility. Furthermore, under 2000 cycles at 30% strain, the devices exhibit highly reproducible electrical behaviour and nearly unchanged gas response signals towards trimethylamine (TMA), NO_2, and NH_3.

Other studies have explored the intrinsic stretchability of PCDTPT, revealing its potential for flexible electronics. Early work by O'Connor et al. [96] demon-

strated that polymer blending can be an effective strategy to improve mechanical compliance. By blending PCDTPT with P3HT at a 1:1 ratio, the resulting composite films were able to sustain strains of up to 75%, while maintaining an enhanced charge carrier mobility of 1.2 cm^2 V^{-1} s^{-1}. Intrinsically stretchable semiconducting composites have been developed by blending PCDTPT with the elastomer SEBS. Tang's group [97] systematically varied the PCDTPT/SEBS composition and identified a weight ratio of 25:75 as optimal, achieving a crack-onset strain of up to 182% and high optical transparency (>95% at 550 nm), while maintaining a charge carrier mobility of 2.31 cm^2 V^{-1} s^{-1}. Further advances were reported by Huo's group [98], who showed that controlling the SEBS microphase-separated structure through a variable-concentration approach can further enhance both charge carrier mobility and crack onset strain, enabling systematic tuning of electrical and mechanical properties.

2.4 Background on flexible temperature sensors

In the early 1960s, researchers began exploiting the temperature-dependent electrical characteristics of semiconductor devices [99]. Diodes and transistors were used for temperature sensing due to the strong temperature dependence of their forward bias voltage drop, with the earliest applications reported by Harris [100] and McNamara [101], demonstrating clear sensitivity to thermal variations through changes in current-voltage behaviour. With the subsequent advancement of complementary metal–oxide–semiconductor (CMOS) technology and the predictable temperature dependence of *p*-*n* junctions and bandgap, silicon became a classical rep-

resentative inorganic material [102, 103]. Benefiting from its oxidation resistance and thermal stability, silicon devices demonstrated high reliability across a wide range of operating conditions and could also withstand high-temperature processes such as doping [104]. Moreover, silicon-based sensors provided a wide temperature range [105,106], ease of integration with on-chip electronics [107], and high sensitivity associated with the temperature coefficient of resistance (TCR) [108].

The advent and rapid development of flexible electronics have exposed the limitations of rigid temperature sensors. Although rigid materials can in some cases be adapted for flexible devices by optimising material design and device architecture [109,110]. However, silicon-based sensors often require complicated fabrication processes [111], which involve high-temperature treatments and energy-intensive deposition techniques. In addition, the inherent rigidity and brittleness of silicon substantially constrain its integration into emerging flexible and wearable electronic applications [112].

Over the past decades, interest has progressively shifted towards organic materials, with organic polymers in particular attracting attention due to their inherently low mechanical stiffness, which makes them one of the most promising platforms for wearable technologies. One of the most important breakthroughs realised with organic semiconductors was the detection of conductivity in conjugated polymers in the late 1970s [42]. For this pivotal discovery, Heeger, MacDiarmid and Shirakawa were awarded the chemistry Nobel prize in the year 2000.

In 2005, a conformable and flexible organic transistor active-matrix sensor network was reported in [113], capable of detecting both pressure and temperature over

large-area flexible substrates. The system employed OFET matrices as switches, with thermistor-based units for temperature sensing, all integrated on a polyimide substrate that is less than 1 mm thick and easy to attach to curved surfaces or even human skin. This paper provided one of the earliest demonstrations of integrating flexible organic temperature sensors into large-area electronic skin systems. Since then, organic temperature sensors have rapidly evolved.

Figure 2.21 outlines several valuable milestones achieved throughout the last decade in the field of flexible temperature sensors.

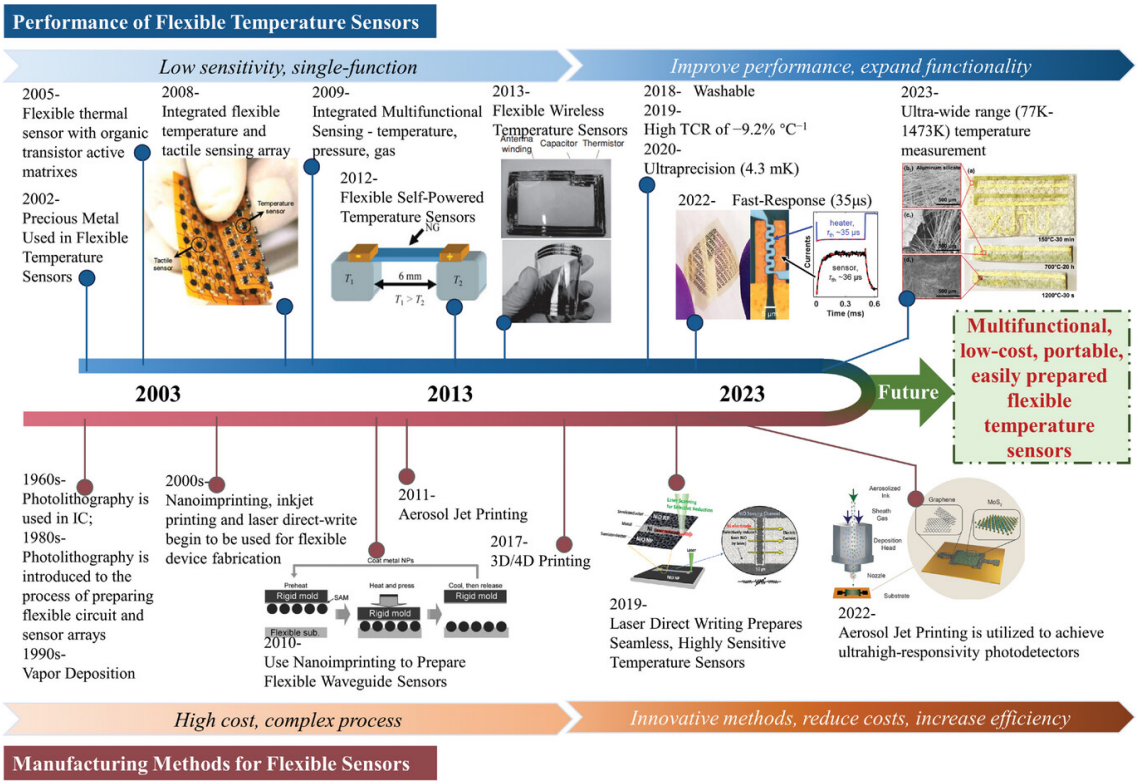

Figure 2.21: Brief timeline of the development of the performance and manufacturing methods of flexible temperature sensors. Reproduced from [114], under the permission of Creative Commons CC BY license.

Along these lines, organic semiconductors have risen as strong candidates that can potentially improve aspects not found on silicon-based sensor technologies, for instance: low-cost fabrication, molecular tunability, and compatibility with large-

area fabrication [115, 116], demonstrating their potential for next-generation wearable and integrated electronic systems.

Electrical conductivity is a key parameter in many organic electronic devices, as high conductivity is a prerequisite for improving their performance for various applications. However, despite significant progress, charge transport in organic semiconductors remains strongly influenced by structural disorder and weak intermolecular coupling, which can limit carrier mobility in thin-film devices [117].

To overcome the challenge of low conductivity, subsequent research has focused on enhancing carrier transport in organic semiconductors through structural engineering, novel polymer design, and doping strategies. For instance, grain-boundary engineering has been shown to effectively modulate charge transport in organic semiconductors [118], where polycrystalline DNTT films with controlled grain sizes exhibited maximised barrier heights when the grain size approached twice the Debye length, resulting in a strong temperature dependence of carrier mobility. In addition, doping strategies have been widely employed to improve thermoelectric performance and electrical conductivity in conjugated polymers. Guo et al. [119] demonstrated enhanced thermoelectric properties in doped PCDTPT-based systems, highlighting the importance of carrier concentration optimisation for temperature-responsive organic devices. At the device level, Ren et al. [120] reported an OTFT integrated with a pentacene thermistor doped with silver nanoparticles, which exhibited enhanced charge transport sensitivity and extended the sensing range to 20 - 70 °C while maintaining low-voltage and low-power operation.

In addition to resistive and thermoelectric sensing approaches based on charge

transport modulation, recent state-of-the-art developments in organic temperature sensing have been increasingly explored in a wide range of fields. For example, optical sensing approaches based on luminescent organic materials have recently emerged as a promising research direction. Sun et al. [121] reported 3D-printable organic phosphorescent materials for real-time thermal sensing and display applications, demonstrating the potential of multifunctional organic thermal sensing systems. Fluorescence-based temperature sensing using flexible organic crystals has also been investigated. Di et al. [122] demonstrated elastically bendable organic crystals capable of optical temperature sensing through temperature-dependent fluorescence variation over a wide temperature range from 77 K to 277 K. Organic phosphorescent materials have been further explored for colourimetric thermal sensing. Si et al. [123] reported corannulene-based phosphorescent materials exhibiting temperature-dependent multiple room-temperature phosphorescence emissions, enabling high colour-resolution thermal sensing. In addition, Liu et al. [124] developed ESIPT-based organic luminescent films for high-temperature optical sensing. The ratiometric thermosensors exhibited a wide sensing range from 40 °C to 300 °C, with a maximum relative sensitivity of 2.5 % K^{-1} at 220 °C.

These studies demonstrate the rapidly expanding range of organic temperature sensing approaches, including phosphorescent, fluorescent, colourimetric, and high-temperature optical sensing systems. Owing to their mechanical flexibility, lightweight nature, and multifunctionality, organic flexible temperature sensors have attracted considerable attention in diverse fields such as healthcare [125, 126], smart wearables [48], automotive manufacturing [127], and robotic tactile sensing [128].

Novel sensing methods and application scenarios continue to emerge [129, 130]. In the following section, materials used as active layers in flexible temperature sensors will be reviewed.

2.5 Temperature sensing Mechanisms

Temperature sensing plays a critical role across a wide range of applications, including healthcare monitoring, wearable electronics, and industrial process control. It refers to the detection of temperature variations and their conversion into electrical signals [17]. As a key physiological parameter, temperature provides important information about the interaction between the human body and the external environment. In particular, accurate skin temperature measurement has been shown to offer valuable insights into cognitive function [131], cardiovascular health [132], and the detection of malignancies [133, 134]. Consequently, temperature sensing is regarded as a fundamental requirement for electronic skin systems [135].

In addition, harsh environments often involve large temperature gradients, mechanical stress, and limited accessibility, which impose stringent requirements on sensor stability, durability, and response time [136, 137]. Conventional rigid sensors may suffer from mechanical mismatch or limited conformability, particularly when integrated onto curved or flexible surfaces [138].

Therefore, flexible temperature sensors based on organic semiconductors offer a promising approach, with the advantages of lightweight, solution processability, and compatibility with large-area fabrication [139]. These advantages make them particularly suitable for emerging applications in distributed sensing and integrated

monitoring systems.

With this background, this section introduces various temperature sensing mechanisms, followed by a focus on organic semiconducting materials, which have emerged as promising candidates for next-generation flexible and wearable temperature sensors [140, 141].

Organic materials have already been integrated as active layers in flexible temperature sensors, offering benefits such as mechanical flexibility [142, 143], low-cost fabrication [144], and tunable electronic properties [145]. These features highlight their potential for future developments in flexible and wearable sensing technologies.

The conductivity of semiconductors is strongly influenced by temperature, primarily due to changes in carrier concentration and mobility. As shown in Equation 2.20, the mobility in disordered organic semiconductors often follows a thermally activated Arrhenius-type relation [146]:

$$\mu(T) = \mu_0 \exp\left(-\frac{\Delta}{kT}\right) \tag{2.20}$$

where μ_0 is the pre-exponential factor, and Δ is the thermal activation energy of the carrier mobility, both of which are material-dependent parameters; k is the Boltzmann constant, and T is the absolute temperature.

According to this equation, carrier mobility increases with rising temperature in disordered organic semiconductors, where transport is governed by thermally activated hopping. This behaviour underpins the operation of many flexible temperature sensing devices. However, carrier mobility in organic semiconductors does not generally follow a simple monotonic dependence on temperature. At higher

temperatures, mobility may decrease due to phonon scattering or traps becoming driving forces [147, 148].

Flexible temperature sensors have been developing towards wearable, highly sensitive, portable, large-area [149], accurate [150], and real-time monitoring trends. These sensors operate by detecting temperature-related variations in the electrical properties of temperature-sensitive materials. Several physical mechanisms have been employed, including resistive sensing, thermocouples, thermochromic effects, and infrared-based detection. The associated physical principles include the thermal resistance effect, Seebeck effect, pyroelectric effect, thermochromism, and infrared radiation absorption, which will be explained in detail later. Each mechanism offers unique advantages depending on the target application, allowing tailored sensor designs to meet specific performance requirements.

2.5.1 Thermal Resistive Temperature Sensors

Thermally activated hopping transport has been widely observed in conjugated polymer systems. Early theoretical work by Vissenberg and Matters established a model for charge transport in disordered organic semiconductors, demonstrating that carrier mobility in such materials is governed by hopping within an exponential density of states distribution and follows a temperature-dependent behaviour [151]. This framework has since been broadly applied to polymer thin-film devices. More generally, Bässler and Köhler comprehensively reviewed charge transport in organic semiconductors and showed that, in structurally disordered films, carrier motion is dominated by thermally activated hopping between localised states rather than

extended band-like transport [41]. Even in high-mobility donor–acceptor polymers, such as the liquid-crystalline system reported by McCulloch et al., mobility retains a measurable temperature dependence in thin-film devices, reflecting the influence of microstructural disorder and intermolecular coupling [152].

The thermal resistance effect is one of the most straightforward and widely used mechanisms for temperature sensors. Resistive temperature sensors, which are applied in flexible temperature sensors, have been widely studied due to their simple architecture, high sensitivity, and compatibility with a wide range of materials [141, 153]. In such sensors, the thermal properties of thermosensitive materials are exploited to convert temperature variations into electrical signals. As the temperature rises, enhanced lattice vibrations lead to stronger carrier scattering, which reduces carrier mobility [154]. In metallic conductors, where the carrier concentration remains approximately constant, this reduction in mobility dominates, increasing resistance.

In disordered organic semiconductors, charge transport is dominated by thermally activated hopping between localised states rather than band-like transport [55, 155]. Charge carriers require thermal energy to hop between neighbouring sites, and the hopping probability increases with temperature [55]. As a result, the effective carrier mobility generally increases with increasing temperature in such systems [72]. Consequently, the enhanced mobility and carrier activation lead to an increase in electrical conductivity and a corresponding decrease in resistance [35].

The temperature coefficient of resistance (TCR) is a key parameter for evaluating the temperature sensitivity of materials. Thermistors are categorised based on the

sign of their TCR: materials with a negative temperature coefficient (NTC) exhibit a decrease in resistance as temperature increases, whereas those with a positive temperature coefficient (PTC) show an increase in resistance with rising temperature.

For resistance temperature detector (RTD) applications, the thermal response of the material is commonly characterised using the following expression for TCR:

$$\alpha = \frac{1}{R\left(T_0\right)} \frac{R\left(T\right) - R\left(T_0\right)}{T - T_0} \tag{2.21}$$

where $R(T)$is the resistance at temperature T, $R(T_0)$ is the initial resistance of the tested sample at temperature T_0. A higher TCR indicates greater temperature sensitivity, which is desirable for high-precision thermal sensing applications [156, 157].

In thermal resistive organic temperature sensors, this thermally activated mobility directly impacts measurable resistance variations. In the present two-terminal PCDTPT devices investigated in this work, the experimentally observed temperature-dependent resistance is therefore primarily attributed to thermally activated hopping transport within the polymer film.

2.5.2 Thermocouple sensors

The thermocouple sensing mechanism is fundamentally based on the Seebeck effect. A thermocouple is a type of temperature sensor that consists of two different thermoelectric elements A and B (typically conductors, semiconductors, or a combination of both) joined at two junctions, shown as in Figure 2.22. When these junctions are exposed to different temperatures, a temperature gradient is

established, and a corresponding voltage is generated due to charge carrier diffusion [158]. This voltage is called the Seebeck voltage, which can be measured and directly correlated to the temperature difference between the junctions.

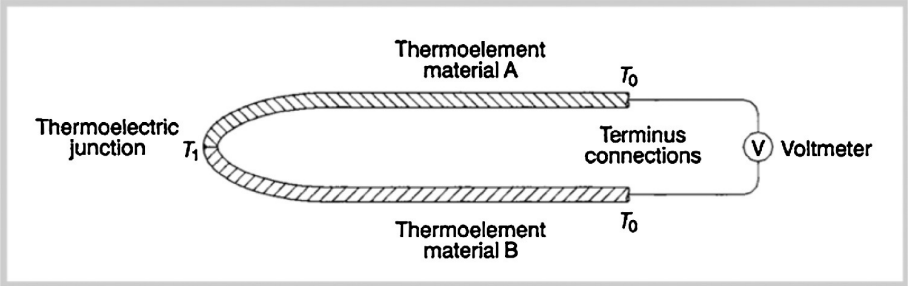

Figure 2.22: Scheme of a thermocouple made of thermoelement A and B [159].

The sensitivity of this effect is quantified by the Seebeck coefficient S, which is defined as the ratio of the thermoelectric voltage generated to the temperature gradient across the material [160]:

$$S = \frac{dV}{dT} \tag{2.22}$$

where dV is the thermoelectric voltage difference, dT is the corresponding temperature difference.

Materials with large Seebeck coefficients are particularly desirable for highly sensitive thermocouple applications. Zhang et al. investigated the influence of RF magnetron sputtering power and gas flow rate on the thermoelectric properties of W–Re TFTCs, revealing that higher sputtering power and optimised gas flow promote the formation of dense, crystalline thin films with enhanced conductivity and reduced signal drift. The fabricated devices achieved a remarkable Seebeck coefficient of 31.1 μV/°C at 1040 °C, outperforming conventional Type-C thermocouples and demonstrating superior stability in high-temperature environments [161]. In

[162], the paper reported a comprehensive assessment of W–Re TFTCs deposited via RF magnetron sputtering, focusing on long-term drift stability and contact resistance. Through optimised annealing conditions, the study achieved lower Seebeck coefficient drift rates and stable performance across repeated thermal cycling, emphasising the significance of post-deposition treatments in maintaining device reliability.

2.5.3 Infrared-based sensing

Infrared-based sensing is a non-contact temperature measurement technique that relies on detecting the infrared radiation naturally emitted by objects as a function of their thermal state. The absorbed thermal radiation is converted into an electrical signal by the IR detector. According to Planck's law, all objects with a temperature above absolute zero emit electromagnetic radiation [163], with spectral radiance described by:

$$B(\lambda, T) = \frac{2hc^2}{\lambda^5} \cdot \frac{1}{e^{\frac{hc}{\lambda k_B T}} - 1} \tag{2.23}$$

where $B(\lambda, T)$ is the spectral radiance at wavelength λ and temperature T, and h, c, and k_B are Planck's constant, the speed of light, and Boltzmann's constant, respectively. This distribution depends not only on temperature but also on the material's emissivity.

The total emitted power per unit area is described by the Stefan–Boltzmann law, stating that the radiated energy P from a surface is [164]:

$$P = \varepsilon \sigma T^4 \tag{2.24}$$

where ε is the emissivity and σ is the Stefan–Boltzmann constant.

By detecting the infrared radiation emitted by an object and applying the above physical laws, the surface temperature can be quantitatively inferred, provided that the emissivity of the material is known.

The ability of infrared thermography (IRT) to perform fast, non-invasive, and remote thermal readings makes infrared sensors highly valuable across industrial [165], aerospace [166,167], and medical applications [168,169]. However, IRT still faces certain limitations. High-quality infrared imaging systems are usually expensive, and their performance is highly sensitive to environmental conditions such as ambient temperature, airflow, and humidity. Consequently, accurate and reliable measurements often require operation within controlled environments to minimise external interferences.

2.6 Summary

This chapter outlined the theoretical background required for this study. It first introduced the fundamental principles of inorganic and organic semiconductors, with emphasis on charge transport and the role of doping. The temperature dependence of conductivity was discussed, particularly the transition from variable-range to nearest-neighbour hopping in disordered systems. Finally, different sensing mechanisms were introduced, providing the conceptual basis for analysing the experimental results in later chapters.

While multiple temperature sensing mechanisms exist, the behaviour investigated in this thesis focuses on resistive sensing, in which resistance variations arise

from thermally activated charge transport processes within the semiconducting layer [67, 72]. The theoretical and experimental analysis presented in the following chapters is therefore grounded in a thermally activated transport framework appropriate for disordered polymer thin films [55].

CHAPTER 3

Materials and Experimental Methods

3.1 Introduction

This chapter describes the materials, fabrication processes, and data collection methods used in this thesis. It begins with the architecture of the organic sensors and the materials employed, followed by the preparation of PCDTPT solutions and the corresponding fabrication processes. Next, the characterisation of organic devices is explained, including measurement techniques and instrumentation.

3.2 Material Studied and device architecture

The organic semiconductor material used in this study is PCDTPT. It is a p-type conjugated polymer with high hole mobility and excellent thermal and chemical sta-

bility [170], making it suitable for application in high-performance organic electronic devices. Its relatively deep HOMO level also facilitates efficient hole injection when paired with appropriate electrode materials [171].

The device architecture consists of three layers: substrate, active layer, and electrode, shown below:

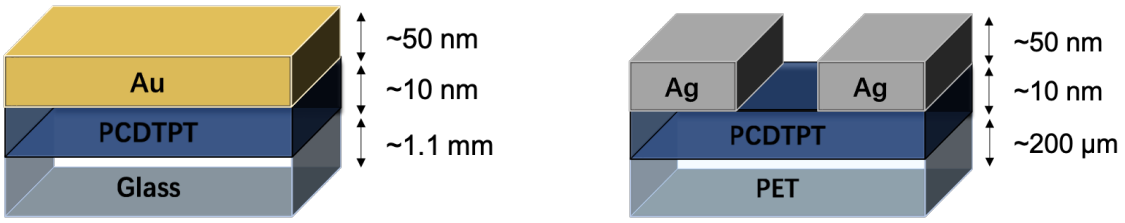

(a) (b)

Figure 3.1: Device architecture of (a) glass substrate and (b) PET substrate from this work.

3.2.1 Sample Preparation

Solution

To prepare the charge transport polymer solutions, PCDTPT was used as the solute and dissolved in chlorobenzene at concentrations of 5, 10, and 15 mg/mL. The mixture was magnetically stirred overnight at room temperature inside a nitrogen-filled glove box to ensure complete dissolution and homogeneity. A Parafilm cover was placed around the cap of the vial to prevent solvent evaporation during stirring.

Because PCDTPT is sensitive to oxygen and water, all fabrication and testing procedures in this project were conducted inside a nitrogen-filled glovebox (MBraun nitrogen glove box). The glovebox environment maintained low levels of oxygen (O_2 < 0.1 ppm) and water vapour ($H_2O < 0.1$ ppm), which can prevent oxidation and degradation, ensuring the stability of the active materials during processing.

Solid State Film

Substrate

There are two substrates applied in this project: polyethylene terephthalate (PET) sheets and glass substrates, both obtained from a commercial company (South China Xiang Science and Technology Co., Ltd. and Thorlabs). The original dimensions of the PET sheets are 210 × 297 mm with a thickness of 200 µm. To be compatible with the shadow mask used during the thermal evaporation process, the PET sheets were cut into 20 × 20 mm squares. The glass substrates were used in their original size of 20 × 20 mm and a thickness of 1.1 mm.

3.2.2 Fabrication Techniques

Once solutions are prepared, active layers can be spin-coated onto the ITO/PET or glass substrate. In this work, spin coating was used to deposit PCDTPT solutions and thermal evaporation was used for the deposition of the metal contact onto the organic layer. A detailed explanation of these fabrication procedures is provided as follows.

Spin Coating

Spin coating is a widely used solution-based process developed for the low-cost deposition of a uniform polymer film in the micrometre to nanometer thickness range [172]. It offers a simple, cost-effective, and scalable approach for fabricating polymer and organic semiconductor layers on various substrates. In this process, a liquid solution is dispensed onto the centre of a substrate, which is then rapidly

rotated at high speed. The film thickness is governed by several parameters and can be estimated according to the expression [172]:

$$h = \left(1 - \frac{\rho_A}{\rho_{A0}}\right) \cdot \left(\frac{3\eta \cdot m}{2\rho_{A0}\omega^2}\right)^{1/3} \tag{3.1}$$

where h is the thickness, ρ_A is the density of the volatile liquid (the mass of volatile solvent per unit volume), ρ_{A0} is the initial volume density, η is the viscosity of the solution, m is the rate of evaporation, and ω is the angular velocity.

In this project, both PET and glass substrates were spin-coated with the active layer solution. For each coating, 100 μL of solution was dispensed onto the substrate and spin-coated at a speed of 2000 rpm for 40 seconds. The choice of this parameter was based on methodology developed in our group and previously reported in [93], where PCDTPT was also used as the active material.

Thermal Annealing

The electrode contacts of the flexible devices fabricated in this study were vapour-deposited onto the solution processed active layers. Thermal annealing is a post-deposition thermal treatment process commonly employed to optimise the structural, morphological, and electrical properties of thin films and polymer layers [173]. This process is typically carried out on a hotplate with a pre-set temperature that is below the melting point of the materials, allowing changes in the orientation of the components, while ensuring uniform heat distribution across the substrate [174].

In this project, each sample was thermally annealed at 150°C for 30 minutes. The choice of this annealing condition was based on a methodology developed in

our group in previous work [93], where PCDTPT was also used as the active material. Following annealing, the samples were placed flat and left in a nitrogen-filled glovebox for one hour to stabilise the film morphology.

Vacuum Thermal Evaporation

Thermal evaporation is a physical vapour deposition technique widely used to deposit thin metal films onto a substrate. The process occurs under high vacuum to minimise contamination and allow free molecular transport of vaporised atoms [175]. In this method, a metal source is placed in a crucible or metal boat made of a high-melting-point material. When the metal reaches its evaporation temperature, the atoms transition from the condensed phase into the vapour phase.

In flexible temperature sensors, a variety of metals are commonly employed as electrode materials, including gold (Au) [176, 177], silver (Ag) [178], copper (Cu) [179], platinum (Pt) [180], and aluminium (Al) [181]. Compared to conventional rigid metal temperature sensors, flexible metal-based sensors offer superior mechanical compliance, enabling them to conform easily to highly curved or dynamic surfaces. This makes them particularly suitable for detecting subtle temperature variations and distributions over small areas.

In this project, silver (Ag) was used as the electrode material for devices fabricated on PET substrates, while gold (Au) was used for glass substrates. This choice was made based on the specific characterisation purposes of each device: gold was selected for the glass substrate devices for X-ray reflectivity (XRR) measurements, as it provides better contrast and stability under X-ray illumination. In contrast, PET substrate devices were used for temperature-dependent electrical measurements. Sil-

ver was chosen for its suitable work function (4.26 eV), which moderately aligns with the HOMO level (5.2 eV) of PCDTPT, promoting hole transport. In addition, silver is a cost-effective electrode material, and it is practical for large-scale or exploratory applications. Both metals were deposited through thermal evaporation under a vacuum of 1.33×10^{-6} mbar, achieving a thickness of 50 nm.

For PET substrates, a shadow mask was employed during deposition to create the electrode pattern, as shown below.

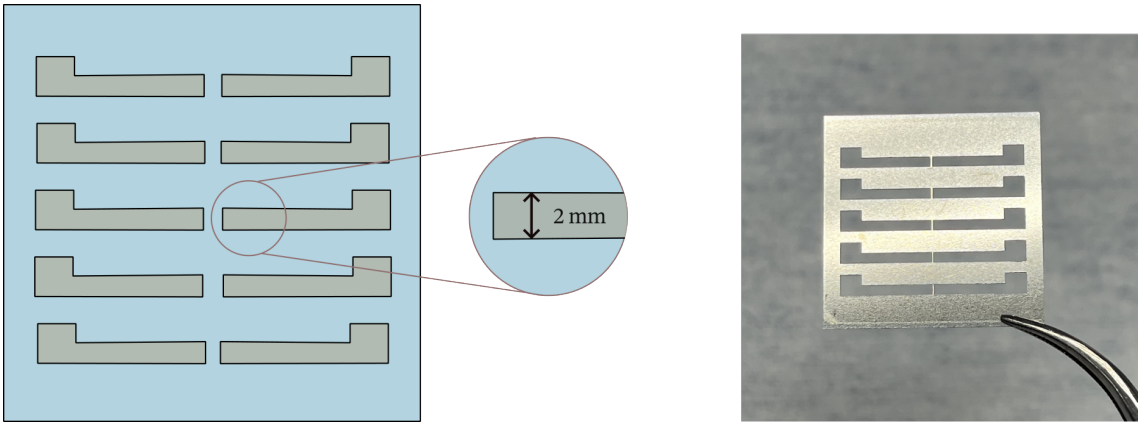

(a) (b)

Figure 3.2: The schematic illustration (a) and photograph (b) of the shadow mask used for Ag deposition.

As the gap between each pair of electrodes varies, this project specifically uses the one with an 80 μm spacing.

This shadow mask was chosen because the rectangular contact areas on both sides facilitate convenient probe placement and ensure reliable, repeatable alignment with the measurement setup. The central gaps between the opposing electrodes provide a clear region through which charge carriers can travel through the organic semiconductor layer. This mask configuration is well suited for evaluating charge transport in two-terminal organic electronic devices.

For glass substrates, a continuous thin layer of gold was deposited without using any mask, covering the entire surface of the substrate.

3.2.3 Electrical Characterisations

Set Up

The experimental setup employed in this study, as illustrated in Figure 3.3a, consists of several key components: a computer for data acquisition and control, an Agilent Technology B1500A semiconductor parameter analyser for current–voltage characterisation, a probe station for precise electrical contact, and a two-terminal device under test. For temperature measurements, a hotplate was used to apply controlled thermal conditions within a nitrogen-filled glovebox to avoid contamination. A camera fixed above the probe station transmitted live images to the computer, to make sure proper contact between the probes and the electrodes, as shown in Figure 3.3b.

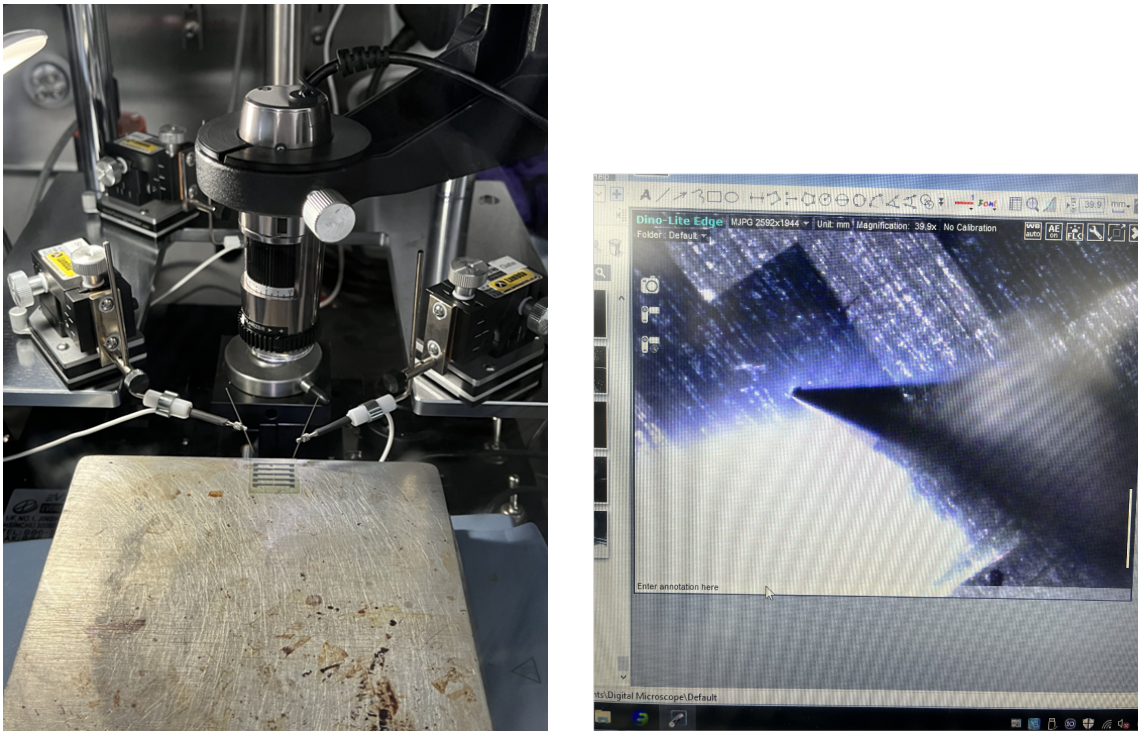

(a) (b)

Figure 3.3: Device characterisations: (a) Experimental setup for temperature-dependent electrical measurements and (b) Camera image during measurements.

I-V Characterisations

During the measurements, a voltage was applied between two silver electrodes, swept from -5 V to $+5$ V to test the electrical resistance of the fabricated device. The experiment was started at room temperature (25°C), and the temperature was subsequently increased in 15°C increments. At each temperature step, the device was placed on a hotplate for 3 minutes, followed by immediate resistance measurement. After each test, the device was removed from the hotplate and placed on a metal surface to cool down for 10 minutes before proceeding to the next temperature step.

3.2.4 Structural Characterisations

X-ray Reflectometry (XRR)

X-ray reflectivity (XRR) is a non-destructive characterisation technique to study the surface and interface properties of thin films and multilayers [182]. The method is based on measuring the intensity of X-rays reflected from the surface of a sample as a function of the incident angle. At shallow angles, total external reflection occurs, and as the angle increases, interference patterns (Kiessig fringes) emerge because of constructive and destructive interference between X-rays reflected at different interfaces within the film. By analysing these interference patterns, information such as film thickness, density, and interface roughness can be extracted precisely [183]. Therefore, XRR is particularly useful for studying smooth, uniform films with thicknesses ranging from a few nanometers to hundreds of nanometers.

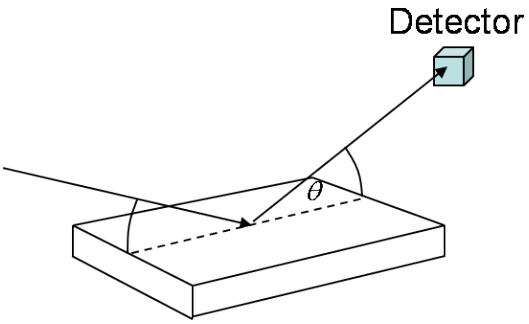

Figure 3.4: Diagram of X-ray specular reflection [184]

The illustration in Fig. 3.4 schematically shows the method of operation for an XRR measurement. When an incident X-ray beam strikes the sample at an angle θ, the detector collects the reflected beam. Deviations from the ideal Fresnel reflectivity, which are caused by interface roughness or compositional variation, enable quantitative analysis of the structural profile normal to the surface.

A thin gold layer was thermally evaporated onto the surface of the PCDTPT film before XRR measurements for the following reasons: Firstly, the measurement sensitivity strongly depends on the contrast in scattering length density (SLD) between adjacent material layers. Organic semiconductors such as PCDTPT typically exhibit low mass density and atomic number, resulting in a low intrinsic SLD. In contrast, Au has a very high atomic number and SLD, making it an ideal material for enhancing interface contrast [185]. Secondly, since PCDTPT is sandwiched between metallic electrodes in the device of this research, adding a gold overlayer in XRR measurements also more accurately represents the operational device structure.

This metallic overlayer serves multiple purposes: it enhances the X-ray reflectivity contrast at the film–air interface by introducing a large SLD discontinuity, enabling clearer Kiessig fringes; it protects the underlying organic semiconductor from oxidation or environmental degradation; and it mimics the actual device structure, where the PCDTPT is typically sandwiched between two electrodes. Additionally, the gold layer may reduce surface roughness effects, thereby improving the accuracy of model-based fitting.

In this study, XRR was employed to obtain the thickness and interfacial roughness of the PCDTPT thin films. By fitting the reflectivity profiles, the structural integrity and morphology of the active layer were analysed in detail, revealing information critical for understanding the correlation between film structure and device performance.

The XRR measurements were conducted by Ben Nicholson in the Department of Physics of Durham University. He also provided the corresponding scattering length

density (SLD) profiles and XRR curves with fitted models for analysis.

3.3 Summary

This chapter described the preparation of PCDTPT thin films and device architectures, along with the experimental techniques used for their fabrication and characterisation. Electrical measurements and X-ray reflectivity were introduced to establish the basis for analysing the structural quality and thermal–electrical behaviour of the devices in the following chapter.

CHAPTER 4

Experimental Results and Discussion

4.1 Introduction

This chapter presents the structural and electrical results of PCDTPT-based flexible devices. It begins with XRR analysis of film thickness and interfacial quality, followed by electrical characterisation examining resistance stability and concentration effects. The temperature dependence of resistance and carrier mobility is then discussed. Together, these results provide insight into the relationship between film structure and thermal–electrical behaviour of the devices.

4.2 XRR Results

The corresponding reflectivity curves and derived scattering length density (SLD) profile were provided for analysis, which was carried out by Dr Ben Nicholson in the Department of Physics of Durham University, shown in Fig. 4.1 and Fig. 4.2.

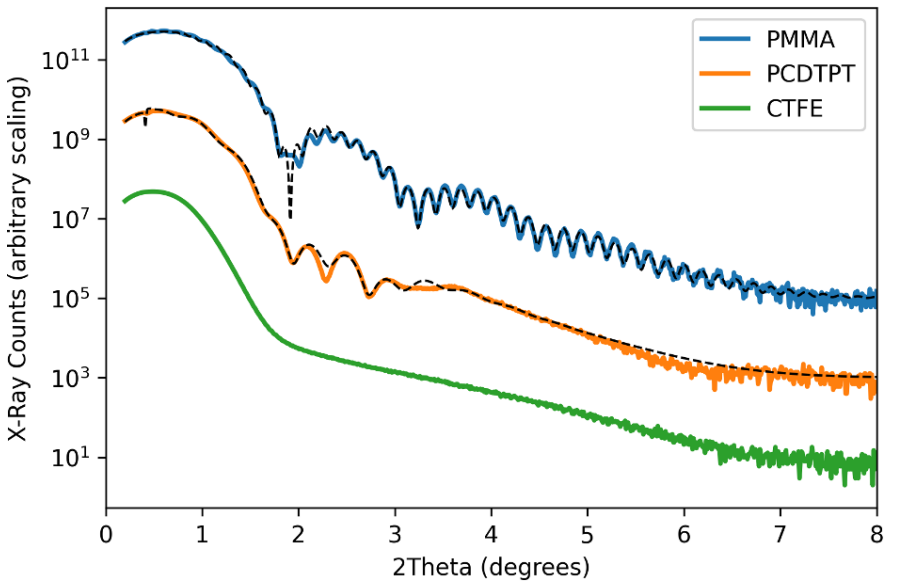

Figure 4.1: XRR curves and fitted models for PMMA, PCDTPT, and CTFE thin films. The coloured solid lines represent the measured data, while the black dashed lines indicate the fitted curves obtained from a multilayer model, which were used to estimate film thickness and interfacial roughness. Only the PCDTPT data are discussed in detail in this work.

The XRR profile of the PCDTPT thin film displays well-defined Kiessig fringes, confirming a relatively uniform and continuous layer, as commonly observed in smooth thin films [186]. These fringes arise from interference between X-rays reflected at different interfaces within the thin film, as discussed in Section 3.2.4. Their periodicity is directly related to the film thickness, while their amplitude provides information on interface quality and density contrast [187].

The gradual decay in fringe amplitude with increasing angle suggests the presence of interfacial roughness or a gradual density transition, consistent with standard

reflectivity theory [188]. The experimental data closely match the fitted model based on the Parratt formalism [189], supporting the validity of the extracted film thickness and scattering length density (SLD) profile, as shown in Figure 4.2.

For context, the figure also shows XRR data for poly(methyl methacrylate)-(PMMA) and poly(chlorotrifluoroethylene)(CTFE). Compared to PMMA, the PCDTPT film exhibits more rapid fringe damping, implying slightly rougher interfaces and potentially lower film density. In contrast to CTFE, PCDTPT shows clearer fringes, suggesting better structural order within the film. Early in this study, the performance of PMMA and CTFE thin films was evaluated alongside PCDTPT. However, due to the poor results obtained with PMMA and CTFE, only PCDTPT was carried forward, and the present discussion focuses exclusively on this material.

The corresponding SLD profiles fitted to the XRR data are shown in Figure 4.2. The horizontal axis (z depth) represents the distance normal to the substrate surface, measured perpendicular to the film plane. The origin (z = 0) corresponds to the glass substrate interface, and increasing z values indicate progression through the PCDTPT layer towards the top Au electrode. The SLD profile therefore reflects the depth-dependent variation in electron density across the glass/PCDTPT/Au multilayer structure. At low z values (below approximately 5 nm), the SLD remains relatively constant, corresponding to the glass substrate. A gradual decrease in SLD is observed at the glass/PCDTPT interface, indicating a finite interfacial roughness rather than an abrupt boundary.

Between approximately 5 nm and 13 nm, the SLD remains relatively low and uniform, corresponding to the PCDTPT layer. The onset of a sharp increase in SLD at

around 13 nm indicates the transition towards the higher-density Au electrode. The SLD reaches a maximum between approximately 18 and 22 nm, which is consistent with the high electron density of the Au layer. The broadened, Gaussian-like shape of this peak suggests a diffused interface between the PCDTPT layer and the Au electrode. Beyond approximately 22 nm, the SLD decreases rapidly, indicating the transition from the Au layer to the ambient environment. Based on the position of the interfaces, the thickness of the PCDTPT layer is estimated to be approximately 10 nm.

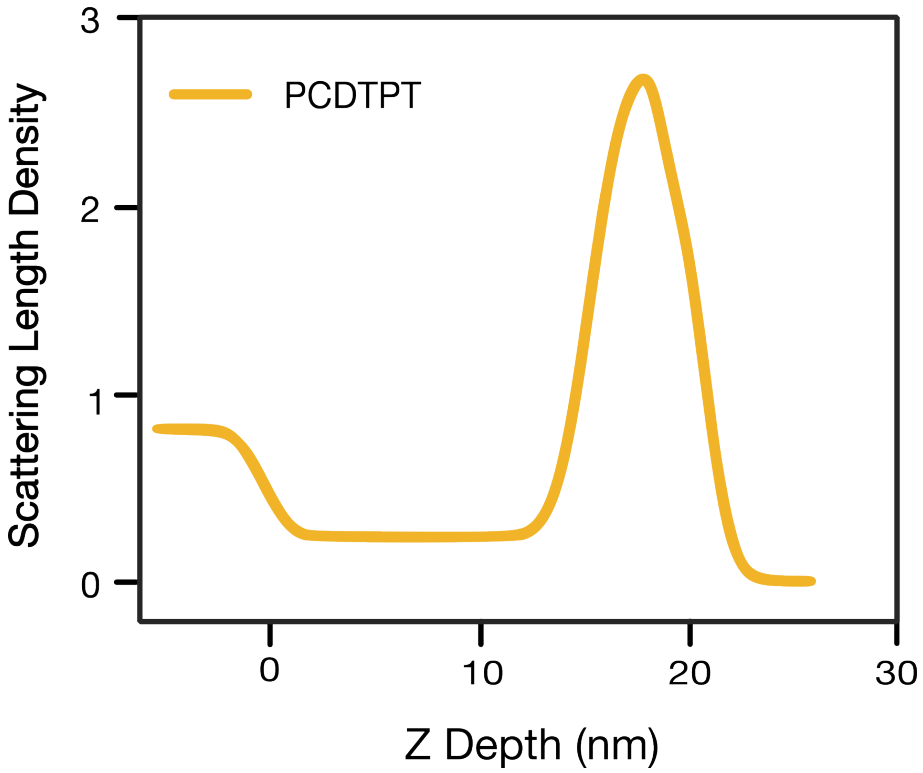

Figure 4.2: SLD profile of the PCDTPT thin film obtained from fitting the XRR data. The z depth axis represents the distance normal to the substrate surface, with $z = 0$ corresponding to the glass substrate interface. The profile illustrates the variation in electron density across the glass/PCDTPT/Au multilayer structure. The PCDTPT layer exhibits a relatively uniform SLD region, while the increase at higher z values corresponds to the Au electrode. The smooth transitions between layers indicate finite interfacial roughness.

In summary, the XRR and SLD analyses confirm that the PCDTPT thin film

forms a continuous and relatively uniform layer with well-defined interfaces, consistent with established thin-film reflectivity behaviour [190]. Although slight interfacial diffusion is indicated by the gradual decay of fringe amplitude, such behaviour is commonly associated with finite interfacial roughness in multilayer reflectivity analysis [191]. Overall, the film demonstrates good structural quality, providing a suitable structural basis for subsequent device fabrication and electrical characterisation.

4.3 Electrical Characterisation Results

The Figure 4.3 below presents the measured resistance values at room temperature for three different solution concentrations (5 mg/mL, 10 mg/mL, and 15 mg/mL). These measurements were performed to verify the accuracy of the resistance readings and to assess the stability of the probe setup.

The figure shows a typical example of the measured raw I–V data. A voltage sweep from –10 V to +10 V was applied to the device with an interval of 0.2 V, and the corresponding current values were recorded (black dots). The data were then fitted with a linear equation in MATLAB (orange line). The slope of the fitted line corresponds to the conductance (in μA/V), and the resistance of the device can be obtained by taking the reciprocal of the slope. This particular device was fabricated with a concentration of 5 mg/mL and measured at a temperature of 25 °C.

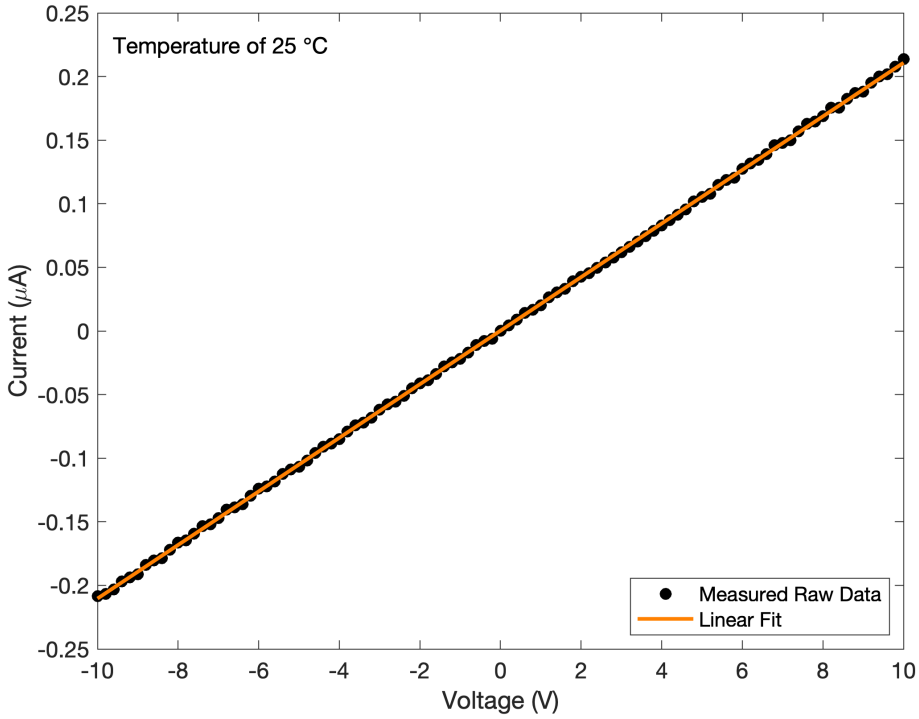

Figure 4.3: I-V characteristics at 25 °C of a device fabricated from a 5 mg/mL PCDTPT solution. The black dots represent the experimental data, and the orange solid line corresponds to a linear fit.

Before the temperature-dependent measurements, each device fabricated from the three different concentrations was measured three times at the initial temperature of 25 °C to verify measurement repeatability and contact stability. As shown in Fig. 4.4, the resistance values are represented by black, red, and blue markers, corresponding to the three consecutive trials. The resistance values were obtained using the measurement procedure described previously. The close overlap of the data points demonstrates minimal variation between repeated measurements for each device, indicating stable electrical contact and reliable measurement conditions. This consistency confirms that subsequent temperature-dependent measurements are not significantly affected by experimental drift or contact-related artefacts.

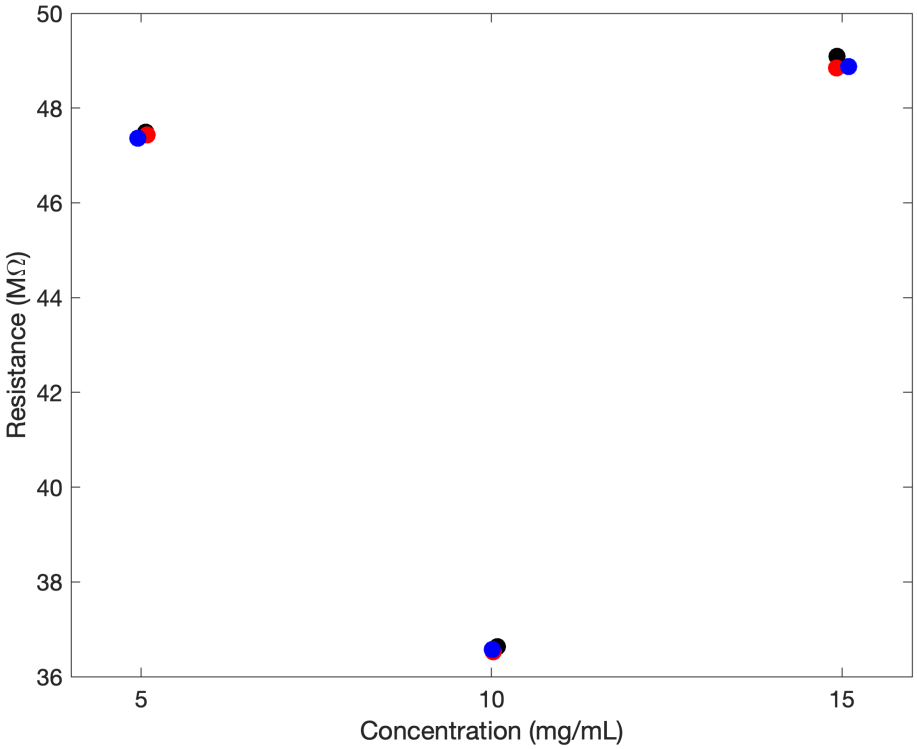

Figure 4.4: Repeated resistance measurements at the starting temperature of 25 °C, performed three times for each device. The black, red, and blue markers represent the first, second, and third measurements, respectively.

The device with a concentration of 10 mg/mL exhibits the lowest resistance, which will be discussed in detail later.

Organic conjugated polymers generally exhibit poor electrical conductivity in their intrinsic (undoped) state. Typically, their conductivities fall within the range of 10^{-10} to 10^{-6}S/cm, that is resistivity between 10^{6}–$10^{10}\Omega \cdot$ cm [192].

To evaluate whether the measured resistance values fall within the expected conductivity range of undoped organic semiconductors, the conductivity σ was calculated using the following relation:

$$\sigma = \frac{L}{R \cdot A} \tag{4.1}$$

where L is the film thickness (in cm), R is the measured resistance (in Ω), and

A is the device area (in cm^2). For the tested device, the film thickness was 10 nm (1×10^{-6} cm), and the channel area was 80 μm $\times$ 2 mm = 1.6×10^{-4} cm^2.

The resistance values ranged from (3.7–4.9) $\times 10^7\,\Omega$, corresponding to conductivities of approximately (1.3–1.7) $\times 10^{-10}$ S/cm, as calculated using Equation 4.1. These values lie within the typical range reported for undoped conjugated polymers, indicating that the measured resistance is consistent with the intrinsic electrical characteristics of organic semiconductors.

To provide a clearer comparison across different concentrations and temperatures, the measured resistance values are summarised in Table 4.1.

Table 4.1: Temperature-dependent resistance of PCDTPT thin films prepared from different solution concentrations (5, 10, and 15 mg/mL).

Temperature (°C)	**5 mg/mL**	**10 mg/mL**	**15 mg/mL**
25	4.75×10^7	3.66×10^7	4.91×10^7
40	2.65×10^7	2.11×10^7	3.01×10^7
55	1.76×10^7	1.41×10^7	1.76×10^7
70	1.10×10^7	9.56×10^6	1.19×10^7
85	7.10×10^6	6.79×10^6	8.46×10^6
100	6.17×10^6	5.76×10^6	7.38×10^6
115	6.12×10^6	4.73×10^6	6.31×10^6
130	1.05×10^7	5.94×10^6	7.28×10^6
145	1.17×10^7	3.36×10^7	3.56×10^7

Based on the data in Table 4.1, Figure 4.5 illustrates the measured resistance as a function of temperature for devices fabricated from solutions with concentrations

of (5 mg/mL, 10 mg/mL, and 15 mg/mL).

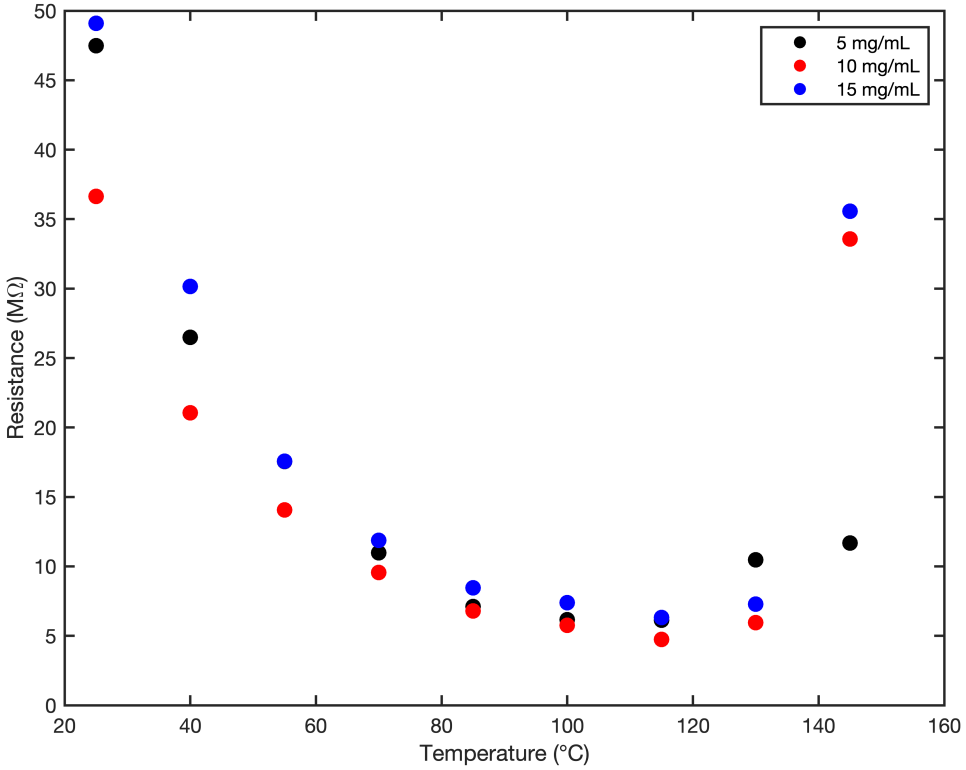

Figure 4.5: Resistance vs. temperature for devices fabricated with 5, 10, and 15 mg/mL solutions.

It is clearly observed that all concentrations exhibit a similar resistance trend with temperature. As the temperature increases up to 115°C, all three samples show a consistent decrease in resistance. However, between 115 °C and 140 °C, a sharp increase in resistance is observed across all samples. After visual inspection using a microscope, metal oxidation and partial electrode delamination were observed. Therefore, the increase in resistance is likely an artefact rather than the intrinsic temperature response of the device. Such degradation is likely to increase the metal–semiconductor contact resistance and reduce the effective contact area, thereby significantly influencing the measured device resistance. Thermally induced

oxidation of metal contacts and interfacial instability in organic electronic devices have been reported to cause substantial resistance increases at elevated temperatures [171, 193].

At a lower temperature range up to around 70°C, the resistance values among the three samples vary significantly, with the 15 mg/mL sample consistently exhibiting the highest resistance in this range. In contrast, within the intermediate temperature range of 70°C to 115°C, the resistance values of all three samples converge and become nearly indistinguishable, indicating that they follow a comparable temperature-dependent resistance trend regardless of concentration in this regime.

A polynomial fit was applied to the resistance data measured between 25–115 °C, to capture the non-linear relationship between resistance and temperature:

$$R(T) = aT^3 + bT^2 + cT + d \tag{4.2}$$

where a, b, and c represent the cubic, quadratic, and linear temperature coefficients of resistance ($\Omega/°C^3$, $\Omega/°C^2$, and $\Omega/°C$, respectively), while d denotes the intercept corresponding to the extrapolated resistance at $T = 0$ °C.

The fitted curve is shown in Figure 4.6.

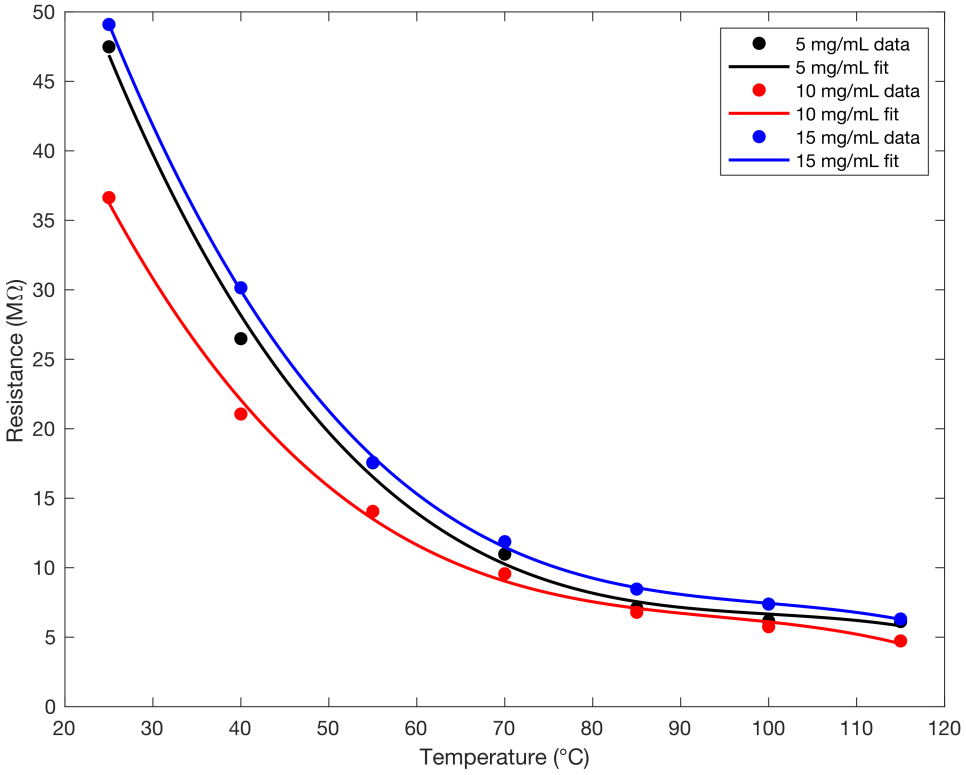

Figure 4.6: Resistance vs. temperature for devices fabricated with 5, 10, and 15 mg/mL solutions with fitted curve.

The temperature coefficient of resistance (TCR) is defined as:

$$\text{TCR} = \frac{1}{R_0} \cdot \frac{dR}{dT} \tag{4.3}$$

When the resistance exhibits a non-linear dependence on temperature, as described by the polynomial fit in Eq. (4.2), the derivative $\frac{dR}{dT}$ becomes temperature dependent. In this case, TCR is no longer a single constant value but varies as a function of temperature. Taking TCR at 25 °C as a reference point, then:

$$\text{TCR} = \frac{a}{R(25°\text{C})} \tag{4.4}$$

The outcomes for different concentrations are illustrated in the following table.

Table 4.2: Temperature Coefficient of Resistance (TCR) at 25 °C for different concentrations.

Concentration	**TCR** ($^{\circ}C^{-1}$)
5 mg/mL	-1.352
10 mg/mL	-1.295
15 mg/mL	-1.352

All samples exhibit negative TCR, indicating that resistance decreases with increasing temperature. The TCR values for the 5 mg/mL and 15 mg/mL devices are very close (approximately $-0.0135\ ^{\circ}C^{-1}$), while the 10 mg/mL device shows a slightly smaller magnitude of $-0.0130\ ^{\circ}C^{-1}$, suggesting a slightly weaker temperature response. A larger absolute value of TCR indicates a stronger sensitivity to temperature variations. This indicates that the variation in concentration may influence the thermal response characteristics of the devices, while the overall trend remains consistent.

Figures 4.7 display the Arrhenius plots of $\ln R$ versus $1/T$ for devices at different concentrations: 5 mg/mL, 10 mg/mL and 15 mg/mL, respectively. Each dataset is represented by a scattered plot covering the temperature range from 25 °C to 115 °C. Linear fits (dashed red lines) were applied only in the interval up to 85 °C, where all three devices exhibited an approximately linear response. The analysis followed the Arrhenius relation:

$$\ln R = \ln R_0 + \frac{E_a}{kT}, \tag{4.5}$$

where E_a is the activation energy (eV), k is the Boltzmann constant (8.617×10^{-5} eV/K), and R_0 represents the hypothetical resistance at infinite temperature, assuming the material continues to follow Arrhenius behaviour. The slope obtained from the linear fit of $\ln(R)$ versus $1/T$ yields the value of E_a/k.

The corresponding Arrhenius plots are shown in Figure 4.7.

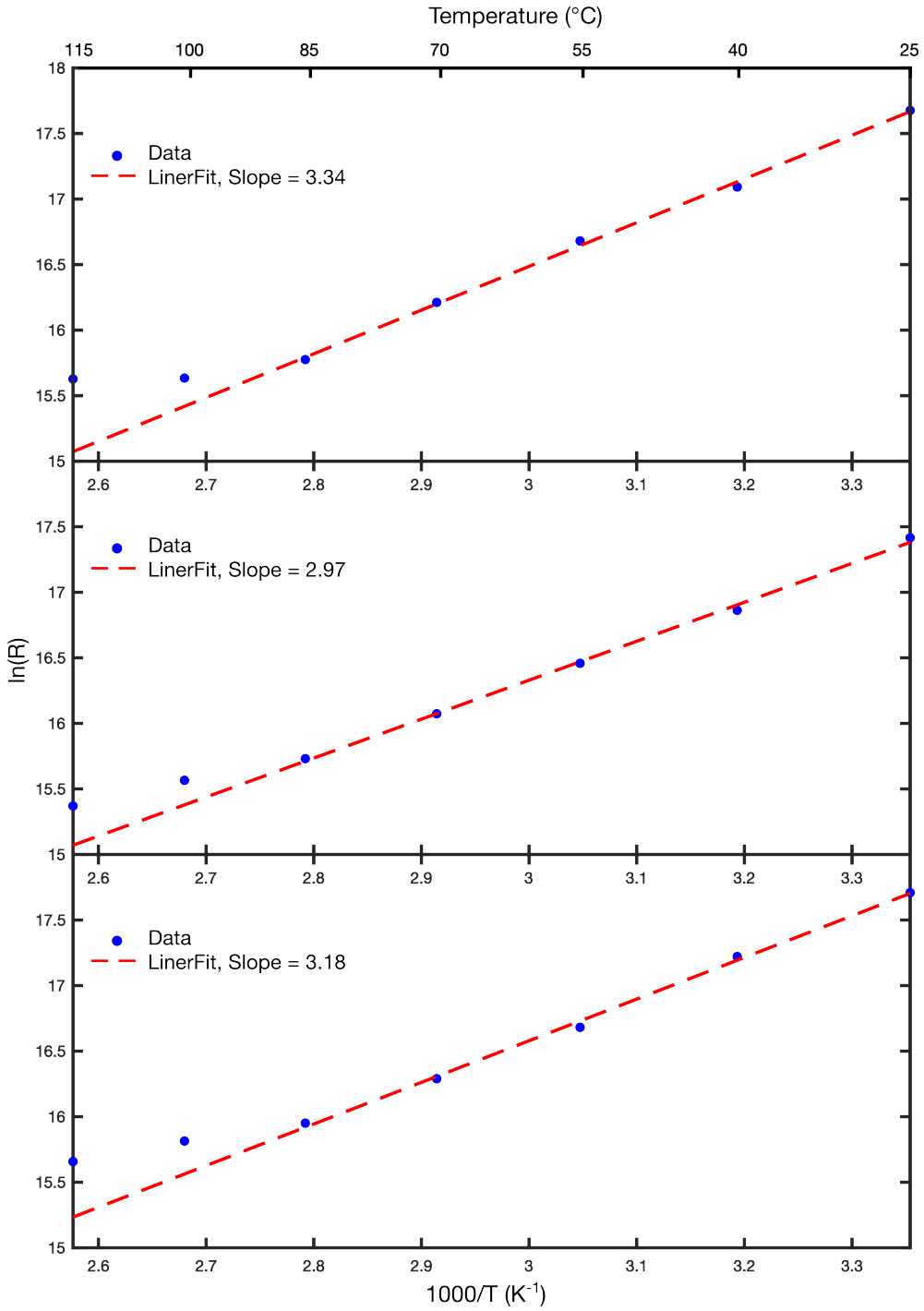

Figure 4.7: Arrhenius plots of resistance $\ln(R)$ versus inverse temperature $(1000/T)$ for devices fabricated from 5, 10, and 15 mg/mL solutions. Experimental data points are taken from 25-115 °C, while linear fittings are performed in the 25–85 °C range.

The activation energy E_a was calculated using Arrhenius fitting:

$$E_a = \text{slope} \times k \tag{4.6}$$

Based on the above equation, the calculated results are summarised in the table below.

Table 4.3: Activation energy E_a calculated from Arrhenius fitting of each concentration.

Concentration (mg/mL)	**Slope**	$\boldsymbol{E_a}$ **(eV)**
5	3.34	0.287
10	2.97	0.256
15	3.18	0.274

The resistance of each device decreases exponentially with increasing temperature, consistent with a thermally activated transport mechanism.

Linear fitting was applied to the data in the 25 °C to 85 °C range to extract the activation energies. Among the three concentrations, the 10 mg/mL device exhibited the lowest activation energy, indicating that charge transport in this device is less thermally activated, possibly due to reduced trap states or a more favourable molecular packing.

Consistent with this, the 10 mg/mL device also shows the lowest resistance at 25 °C and the smallest magnitude of TCR, implying that charge carriers in this film encounter lower energetic barriers and that the transport is less sensitive to temperature variations [46,55,151]. Such behaviour may be associated with a higher intrinsic carrier concentration or improved film morphology compared with the other

concentrations.

The observed variation in activation energy and resistance may be attributed to the concentration of the polymer solution used in 10 mg/mL device fabrication. Higher concentrations can enhance molecular packing and improve film continuity, thereby reducing energetic disorder [44, 46, 152]. However, it is difficult to rule out the possibility that the differences arise from random fluctuations in the fabrication process, such as local inhomogeneities, minor differences in spin-coating conditions, or electrode contact variability. Further statistical analysis across multiple devices would be required to distinguish systematic concentration effects from process-induced variability.

However, it should be noted that the analysis is based on a single device for each concentration. Therefore, the observed differences in conductivity and mobility may partially result from random fluctuations or fabrication-related variability rather than concentration alone [46, 193, 194].

4.4 Conclusion

This chapter presented the structural and electrical characterisation of PCDTPT thin-film devices fabricated from three solution concentrations (5, 10, and 15 mg/mL). XRR analysis confirmed the formation of continuous films with well-defined interfaces, consistent with established thin-film reflectivity behaviour [186]. Electrical measurements revealed thermally activated transport behaviour in the 25–115 °C range, in agreement with hopping-dominated transport models reported for disordered conjugated polymers [55, 151].

Among the three concentrations, the 10 mg/mL device exhibited the lowest activation energy, lowest resistance at room temperature, and smallest TCR magnitude, suggesting reduced energetic disorder and improved charge transport, consistent with morphology–transport correlations reported in conjugated polymer systems [46].

At temperatures above approximately 115 °C, a sharp increase in resistance was observed for all devices. Visual inspection indicated electrode oxidation and partial delamination, suggesting that interfacial degradation dominates the electrical response in this regime. This suggests the upper operational temperature limit of the present device architecture.

Overall, the results demonstrate that solution concentration significantly influences device performance, while also highlighting the role of interfacial stability in determining high-temperature behaviour.

It should be noted that the electrical characterisation presented in this study is based on a limited number of devices, with a single representative sample analysed for each concentration. While repeated measurements confirmed good short-term reproducibility at the device level, broader statistical validation across multiple independently fabricated samples would be required to establish quantitative trends with greater confidence.

CHAPTER 5

Conclusion and Future Work

5.1 Conclusion

This thesis has explored the thermal–electrical properties of PCDTPT thin films fabricated on flexible substrates. Through X-ray reflectivity, the films were shown to possess moderately uniform interfaces, providing a stable foundation for charge transport. Temperature-dependent resistance measurements demonstrated a clear thermal response, highlighting the strong influence of film morphology, interfacial quality, and concentration on device behaviour.

Among the devices studied, the film prepared from a 10 mg/mL solution exhibited the lowest resistance at 25 °C, the smallest activation energy, and the least temperature-dependent variation in resistance (lowest magnitude of TCR). These

results suggest that an intermediate concentration produces a more favourable morphology balance, simultaneously ensuring sufficient film continuity while avoiding excessive aggregation or disorder, thereby optimising charge transport pathways. By contrast, both lower (5 mg/mL) and higher (15 mg/mL) concentrations may introduce structural inhomogeneity that reduces conductivity and stability.

However, these conclusions are based on measurements of a single device at each concentration. The observed variations may therefore come from random factors, such as local inhomogeneities, spin-coating variability, or contact resistance between the probe and the electrode. More extensive and repeated studies on larger device sets will be necessary to establish statistically reliable conclusions.

Overall, this work establishes the link between thin-film structure and thermally activated electrical behaviour in PCDTPT-based devices. The findings are evident that optimisation of material processing is critical for achieving sensitive and stable flexible temperature sensors. More broadly, the results demonstrate the potential of intrinsic polymer as an active material for applications in flexible organic electronics.

5.2 Future Work

Three approaches are proposed that can potentially increase performance and provide deeper insights into the morphology of flexible organic sensors.

(1)Thickness Optimisation and Morphology Control: The estimated PCDTPT film thickness and corresponding Kiessig fringe periodicity indicate a moderately uniform active layer. Future work can use atomic force microscopy (AFM) to examine the topographical features, surface roughness, and possible phase separation

in PCDTPT films, to understand and establish correlations between these morphological characteristics and device performance.

(2)Quantitative Carrier Density Characterisation via Hall Effect Measurements: While current electrical measurements provide valuable insight into the device resistance and transport behaviour, they do not directly yield carrier concentration values. Conducting Hall effect measurements will allow precise observation of the carrier density and mobility, thereby understanding charge transport mechanisms in PCDTPT films.

(3)Improving Device Stability for Ambient Operation: Currently, all fabrication and characterisation steps are carried out within glovebox environment due to the air sensitivity of PCDTPT. To expand the practical situations of devices, future research should explore strategies to enhance the stability of working under air, such as encapsulation techniques and incorporation of stabilising additives.

Overall, the future work will involve further experimental investigations to understand the structural and functional performance of PCDTPT. These efforts will contribute to advancing the field of organic devices and further the potential in various applications.

Bibliography

[1] J. A. Rogers, T. Someya, and Y. Huang, "Materials and mechanics for stretchable electronics," *Science*, vol. 327, no. 5973, pp. 1603–1607, 2010.

[2] J. Heikenfeld, A. Jajack, J. A. Rogers, P. Gutruf, L. Tian, T. Pan, R. Li, M. Khine, J. Kim, J. Wang, and J. Kim, "Wearable sensors: modalities, challenges, and prospects," *Lab on a Chip*, vol. 18, no. 2, pp. 217–248, 2018.

[3] X. Wang, Z. Liu, and T. Zhang, "Nanomaterial-enabled wearable sensors for healthcare," *Advanced Functional Materials*, vol. 27, no. 8, p. 1605594, 2017.

[4] B. Zhao, H. Zhang, Y. Miao, Z. Wang, L. Gao, H. Wang, Y. Hao, and W. Li, "High color stability and cri ($>$ 80) fluorescent white organic light-emitting diode based pure emission of exciplexes by employing merely complementary colors," *Journal of Materials Chemistry C*, vol. 6, pp. 304–311, 2018.

[5] R. Wei, H. Li, Z. Chen, X. Wang, M. Zhang, J. Liu, F. Zhou, and L. Xu, "Revolutionizing wearable technology: advanced fabrication techniques for body-conformable electronics," *npj Flexible Electronics*, vol. 8, p. 83, 2024.

[6] Z. Zhang, Y. Wang, T. Cai, B. Wu, B. Hu, X. Li, E. Song, G. Huang, Z. Tian, Z. Di, and Y. Mei, "Recent progress on flexible silicon nanomembranes for advanced electronics and optoelectronics," *Advanced Functional Materials*, Apr. 2025.

[7] A. Toubal, B. Bengherbia, M. Ould Zmirli, and A. Guessoum, "Fpga implementation of a wireless sensor node with built-in security coprocessors for secured key exchange and data transfer," *Measurement*, vol. 153, p. 107429, 2020.

[8] J. B. Kaushal, P. Raut, and S. Kumar, "Organic electronics in biosensing: A promising frontier for medical and environmental applications," *Biosensors*, vol. 13, p. 976, Nov. 2023.

[9] H. W. Song, W. Choi, T. Jeon, and J. H. Oh, "Recent advances in smart organic sensors for environmental monitoring systems," *ACS Applied Electronic Materials*, vol. 5, no. 1, pp. 77–99, 2023.

[10] D.-H. Kim, J.-H. Ahn, W. M. Choi, , *et al.*, "Materials and mechanics for stretchable electronics," *Science*, vol. 327, no. 5973, pp. 1603–1607, 2010.

[11] D.-H. Kim, N. Lu, R. Ma, Y.-S. Kim, R.-H. Kim, S. Wang, J. Wu, S. M. Won, H. Tao, A. Islam, K. J. Yu, T. I. Kim, R. Chowdhury, M. Ying, L. Xu, M. Li, H.-J. Chung, H. Keum, M. McCormick, P. Liu, Y.-W. Zhang, F. G. Omenetto, Y. Huang, T. Coleman, and J. A. Rogers, "Epidermal electronics," *Science*, vol. 333, no. 6044, pp. 838–843, 2011.

[12] J. Kim, M. Lee, H. J. Shim, R. Ghaffari, H. R. Cho, D. Son, Y. H. Jung, M. Soh, C. Choi, S. Jung, K. Chu, D. Jeon, S.-T. Lee, J. H. Kim, S. H. Choi, T. Hyeon, and D.-H. Kim, "Stretchable silicon nanoribbon electronics for skin prosthesis," *Nature Communications*, vol. 5, p. 5747, 2014.

[13] S. Khan, L. Lorenzelli, and R. S. Dahiya, "Technologies for printing sensors and electronics over large flexible substrates: A review," *IEEE Sensors Journal*, vol. 15, no. 6, pp. 3164–3185, 2015.

[14] H. Park, S. Kim, J. Lee, I. Lee, S. Bontapalle, Y. Na, and K. Sim, "Organic flexible electronics with closed-loop recycling for sustainable wearable technology," *Nature Electronics*, vol. 7, pp. 39–50, 2024.

[15] J. Cai, M. Du, and Z. Li, "Flexible temperature sensors constructed with fiber materials," *Advanced Materials Technologies*, vol. 7, p. 2101182, 2022.

[16] S. Lim and J. W. Suk, "Flexible temperature sensors based on two-dimensional materials for wearable devices," *Journal of Physics D: Applied Physics*, vol. 56, no. 6, p. 063001, 2023.

[17] Q. Li, L. N. Zhang, X. Tao, and X. Ding, "Review of flexible temperature sensing networks for wearable physiological monitoring," *Advanced Healthcare Materials*, vol. 6, no. 16, p. 1601371, 2017.

[18] L. Liu, S. Niu, J. Zhang, Z. Mu, J. Li, B. Li, X. Meng, C. Zhang, Y. Wang, T. Hou, Z. Han, S. Yang, and L. Ren, "Bioinspired, omnidirectional and hypersensitive flexible strain sensors," *Advanced Materials*, vol. 34, no. 2200823, 2022.

[19] B. A. Kuzubaşoğlu and S. K. Bahadır, "Flexible temperature sensors: A review," *Sensors and Actuators A: Physical*, vol. 315, p. 112282, Nov. 2020.

[20] P. C. Chow and T. Someya, "Organic photodetectors for next-generation wearable electronics," *Advanced Materials*, vol. 32, no. 15, p. 1902045, 2020.

[21] X.-F. Teng, Y.-T. Zhang, C. C. Y. Poon, and P. Bonato, "Wearable medical systems for p-health," *IEEE Reviews in Biomedical Engineering*, vol. 1, pp. 62–74, 2008.

[22] Kenry, J. C. Yeo, and C. T. Lim, "Emerging flexible and wearable physical sensing platforms for healthcare and biomedical applications," *Microsystems & Nanoengineering*, vol. 2, p. 16043, 2016.

[23] J.-S. Kim, D. I. Kim, J. H. Kim, S. Lee, Y.-W. Kim, S. H. Lee, K. Cho, and C. Park, "Intrinsically stretchable subthreshold organic transistors for highly sensitive low-power skin-like active-matrix temperature sensors," *Advanced Functional Materials*, vol. 33, no. 36, p. 2305252, 2023.

[24] M. Jung, S. Jeon, and J.-M. Bae, "Scalable and facile synthesis of stretchable thermoelectric fabric for wearable self-powered temperature sensors," *RSC Advances*, vol. 8, no. 56, pp. 32000–32007, 2018.

[25] Y. Lu, H. Zhang, Y. Zhao, H. Liu, Z. Nie, F. Xu, J. Zhu, and W. Huang, "Robust fiber-shaped flexible temperature sensors for safety monitoring with ultrahigh sensitivity," *Advanced Materials*, vol. 36, no. 18, p. e2310613, 2024.

[26] G. Oh, Y. Kim, J. Lee, M. Kim, S. M. Park, H. J. Lee, and H. Kwon, "Integrated temperature–humidity sensors for a pouch-type battery using 100% printing process," *Sensors*, vol. 24, no. 1, p. 104, 2024.

[27] M. Yuan, B. Li, M. Wu, B. Wang, J. Sun, Y. Huang, and M. Zhu, "Recent progress of energy-storage-device-integrated sensing systems for wearable electronics," *Nanomaterials*, vol. 13, no. 4, p. 645, 2023.

[28] N. Lu, N. Gao, L. Li, M. Liu, W. Xie, Y. Xu, Y. Zhang, L. Wang, and E. Wang, "Temperature, electric-field, and carrier-density dependence of hopping magnetoresistivity in disordered organic semiconductors," *Physical Review B*, vol. 96, no. 16, p. 165205, 2017.

[29] I. I. Fishchuk, A. Kadashchuk, M. Ullah, J. Genoe, H. Bässler, V. Karpus, E. Böhler, H. Sitter, U. Scherf, and V. I. Arkhipov, "Temperature dependence of the charge carrier mobility in disordered organic semiconductors at large carrier concentrations," *Physical Review B*, vol. 81, no. 4, p. 045202, 2010.

[30] M. Koopmans, A. J. J. M. van Breemen, N. Lu, J. J. Michels, and R. Coehoorn, "Electrical conductivity of doped organic semiconductors," *ACS Applied Materials & Interfaces*, vol. 12, no. 41, pp. 46057–46065, 2020.

[31] A. Hofacker, B. Rössner, H. Kleemann, T. Menke, A. Fischer, K. Leo, and B. Lussem, "Critical charge transport networks in doped organic semiconductors," *Communications Materials*, vol. 1, no. 1, p. 88, 2020.

[32] Lumen Learning, "Lattice structures in crystalline solids." Chemistry: Atoms First – Liquids and Solids module. Accessed: 20 August 2025.

[33] D. Kumar and M. Johari, "Characteristics of silicon crystal, its covalent bonding and their structure, electrical properties, uses," in *AIP Conference Proceedings*, vol. 2220, p. 040037, 2020.

[34] ChemicalBook Editorial Team, "Diamond: Crystal structure, uses." https://www.chemicalbook.com/article/diamond-crystal-structure-uses.htm, 2024. Accessed: 20 August 2025.

[35] D. A. Neamen, *Semiconductor Physics and Devices: Basic Principles*. New York: McGraw-Hill Education, 4th ed., 2012.

[36] D. A. Neamen, *Semiconductor Physics and Devices: Basic Principles*. New York: McGraw-Hill Education, 4th ed., 2012. Eq. (3.72).

[37] Dissemination of IT for the Promotion of Materials Science (DoITPoMS), "Behaviour of the chemical potential in semiconductors." https://www.doitpoms.ac.uk/tlplib/semiconductors/chemical_potential.php, 2025. Accessed: 20 August 2025.

[38] S. M. Sze and K. K. Ng, *Physics of Semiconductor Devices*. Hoboken, NJ: Wiley-Interscience, 3rd ed., 2006.

[39] DevXplained, "P–n junction." https://devxplained.eu/en/blog/p-n-junction, 2020.

[40] Z. Moradi, S. Z. Jahromi, and M. Ghaedi, "Design of active photocatalysts and visible light photocatalysis," in *Photocatalysis: Fundamental Processes and Applications*, vol. 32 of *Interface Science and Technology*, pp. 557–623, Elsevier, 2021.

[41] H. Bässler and A. Köhler, "Charge transport in organic semiconductors," *Chemical Reviews*, vol. 115, no. 23, pp. 12611–12673, 2015.

[42] T. Ito, H. Shirakawa, and S. Ikeda, "Simultaneous polymerization and formation of polyacetylene film on the surface of concentrated soluble ziegler-type catalyst solution," *Journal of Polymer Science: Polymer Chemistry Edition*, vol. 12, no. 1, pp. 11–20, 1974.

[43] C. K. Chiang, J. Fincher, C. R., Y. W. Park, A. J. Heeger, H. Shirakawa, E. J. Louis, S. C. Gau, and A. G. MacDiarmid, "Electrical conductivity in doped polyacetylene," *Phys. Rev. Lett.*, vol. 39, no. 17, pp. 1098–1101, 1977.

[44] Y. Li, "Molecular design of photovoltaic materials for polymer solar cells: Toward suitable electronic energy levels and broad absorption," *Accounts of Chemical Research*, vol. 45, no. 5, pp. 723–733, 2012.

[45] A. Facchetti, "π-conjugated polymers for organic electronics and photovoltaic cell applications," *Chemistry of Materials*, vol. 23, no. 3, pp. 733–758, 2011.

[46] R. Noriega, J. Rivnay, K. Vandewal, F. P. V. Koch, N. Stingelin, D. M. DeLongchamp, and A. Salleo, "A general relationship between disorder, aggregation and charge transport in conjugated polymers," *Nature Materials*, vol. 12, pp. 1038–1044, 2013.

[47] H. Sirringhaus, "25th anniversary article: Organic field-effect transistors: The path beyond amorphous silicon," *Advanced Materials*, vol. 26, no. 9, pp. 1319–1335, 2014.

[48] T. Someya, Z. Bao, and G. G. Malliaras, "The rise of plastic bioelectronics," *Nature*, vol. 540, no. 7633, pp. 379–385, 2016.

[49] Nagwa, "Hybridization of atomic orbitals." `https://www.nagwa.com/en/explainers/384125736467/`, n.d.

[50] "sp^2 hybrid orbital." `https://glossary.periodni.com/glossary.php?en=sp2%2Bhybrid%2Borbital`.

[51] A. Köhler and H. Bässler, *Electronic Processes in Organic Semiconductors: An Introduction*. Weinheim: Wiley-VCH, 2015.

[52] V. Podzorov *et al.*, "High-mobility field-effect transistors based on transition metal phthalocyanine single crystals," *Applied Physics Letters*, vol. 82, no. 11, pp. 1739–1741, 2003.

[53] M. Oehzelt, N. Koch, and G. Heimel, "Organic semiconductor density of states controls the energy level alignment at electrode interfaces," *Nature Communications*, vol. 5, no. 4174, 2014.

[54] D. Qin, J. Chen, and N. Lu, "A novel density of states (dos) for disordered organic semiconductors," *Micromachines*, vol. 14, no. 7, p. 1433, 2023.

[55] H. Bässler, "Charge transport in disordered organic photoconductors: A monte carlo simulation study," *Physica Status Solidi (b)*, vol. 175, no. 1, pp. 15–56, 1993.

[56] X. Zhu, G.-H. Kim, and K. P. Pipe, "Doping in organic semiconductors," *Chemical Reviews*, vol. 116, no. 21, pp. 12174–12235, 2016.

[57] X. Crispin, S. Marciniak, W. Osikowicz, G. Zotti, A. W. D. van der Gon, F. Louwet, M. Fahlman, L. Groenendaal, M. P. de Jong, and W. R. Salaneck, "The origin of the high conductivity of poly(3,4-ethylenedioxythiophene)–poly(styrenesulfonate) (pedot–pss) plastic electrodes," *Journal of the American Chemical Society*, vol. 126, no. 39, pp. 11889–11899, 2004.

[58] B. Lüssem, M. Riede, and K. Leo, "Doping of organic semiconductors," *Physica Status Solidi (a)*, vol. 210, no. 1, pp. 9–43, 2013.

[59] Z. Yao, S. Wang, S. Wang, A. Tang, C. Wang, and Z. Wei, "N-dmbi as a powerful n-type dopant in organic semiconductors," *Advanced Materials*, vol. 30, no. 24, p. 1800006, 2018.

[60] N. Koch, "The electronic structure of organic semiconductor interfaces: Energetics of charge injection layers," *Journal of Physics: Condensed Matter*, vol. 25, no. 9, p. 094002, 2013.

[61] A. Lucia, A. Savva, P. A. Patsalas, and T. D. Anthopoulos, "High-performance solution-processed organic thermoelectric materials through molecular design," *Advanced Materials*, vol. 29, no. 45, p. 1606712, 2017.

[62] Y. Zeng, W. Zheng, Y. Guo, G. Han, and Y. Yi, "Doping mechanisms of n-dmbi-h for organic thermoelectrics: hydrogen removal vs. hydride transfer," *Journal of Materials Chemistry A*, vol. 8, no. 16, pp. 8323–8328, 2020.

[63] I. Fishchuk, A. Kadashchuk, M. Ullah, H. Sitter, A. Pivrikas, J. Genoe, and H. Bässler, "Electric field dependence of charge carrier hopping transport within the random energy landscape in an organic field effect transistor," *Physical Review B*, vol. 86, no. 4, p. 045207, 2012.

[64] S. Morab, M. M. Sundaram, and A. Pivrikas, "Review on charge carrier transport in inorganic and organic semiconductors," *Materials*, vol. 15, no. 11, p. 3903, 2022.

[65] A. J. Heeger, S. Kivelson, J. R. Schrieffer, and W. P. Su, "Solitons in conducting polymers," *Reviews of Modern Physics*, vol. 60, no. 3, pp. 781–850, 1988.

[66] J. Cottaar, F. J. W. van den Berg, R. Coehoorn, and P. A. Bobbert, "Scaling theory for percolative charge transport in disordered molecular semiconductors," *Physical Review Letters*, vol. 107, no. 13, p. 136601, 2011.

[67] V. Coropceanu, J. Cornil, D. A. da Silva Filho, Y. Olivier, R. Silbey, and J.-L. Brédas, "Charge transport in organic semiconductors," *Chemical Reviews*, vol. 107, no. 4, pp. 926–952, 2007.

[68] N. Mott, "Conduction in non-crystalline materials: Iii. localized states in a pseudogap and near extremities of conduction and valence bands," *Philosophical Magazine*, vol. 19, no. 160, pp. 835–852, 1969.

[69] X. Wang, L. F. Register, and A. Dodabalapur, "Redefining the mobility edge in thin-film transistors," *Physical Review Applied*, vol. 11, no. 6, p. 064039, 2019.

[70] M. Tripathi, R. Giridharagopal, L. Gundlach, and D. S. Ginger, "Correlating side-chain-induced molecular orientations and bulk charge transport in donor–acceptor copolymers," *Applied Physics Letters*, vol. 112, no. 6, p. 063301, 2018.

[71] M. N. Gueye, A. Carella, J. Faure-Vincent, R. Demadrille, and J.-P. Simonato, "Progress in understanding structure and transport properties of pedot-based materials: A critical review," *Progress in Materials Science*, vol. 108, p. 100616, 2020.

[72] N. Tessler, Y. Preezant, N. Rappaport, and Y. Roichman, "Charge transport in disordered organic materials and its relevance to thin-film devices: A tutorial review," *Advanced Materials*, vol. 21, no. 27, pp. 2741–2761, 2009.

[73] A. M. Nardes, M. Kemerink, and R. A. J. Janssen, "Anisotropic hopping conduction in spin-coated pedot:pss thin films," *Physical Review B*, vol. 77, no. 11, p. 115204, 2008.

[74] M. Pei, J. Guo, B. Zhang, S. Jiang, Z. Hao, X. Xu, and Y. Li, "Semiconductor/dielectric interface in organic field-effect transistors: charge transport, interfacial effects, and perspectives with 2d molecular crystals," *Advances in Physics: X*, vol. 5, no. 1, p. 1747945, 2020.

[75] S. D. Baranovskii, "Theoretical description of charge transport in disordered organic semiconductors," *physica status solidi (b)*, vol. 251, no. 3, pp. 487–525, 2014.

[76] Y.-J. Cheng, S.-H. Yang, and C.-S. Hsu, "Synthesis of conjugated polymers for organic solar cell applications," *Chemical Reviews*, vol. 109, no. 11, pp. 5868–5923, 2009.

[77] S. Ren, Z. Wang, W. Zhang, Y. Ding, and Z. Yi, "Donor-acceptor-based organic polymer semiconductor materials to achieve high hole mobility in organic field-effect transistors," *Polymers*, vol. 15, no. 18, p. 3713, 2023.

[78] C. Yang, B. Cheng, J. Xu, J. Yu, and S. Cao, "Donor-acceptor-based conjugated polymers for photocatalytic energy conversion," *Energy & Environmental Chemistry*, 2023.

[79] C. Cheng, J. Yu, D. Xu, L. Wang, G. Liang, L. Zhang, and M. Jaroniec, "In-situ formatting donor-acceptor polymer with giant dipole moment and ultrafast exciton separation," *Nature Communications*, vol. 15, p. 1313, 2024.

[80] I. Jalan, C. F. N. Marchiori, Z. Genene, A. Johansson, M. Araujo, E. Wang, J. van Stam, and E. Moons, "Donor-acceptor polymer complex formation in solution confirmed by spectroscopy and atomic-scale modelling," *Journal of Materials Chemistry C*, 2021.

[81] S. L. Fronk, M. Wang, M. Ford, J. Coughlin, C.-K. Mai, and G. C. Bazan, "Effect of chiral 2-ethylhexyl side chains on chiroptical properties of the narrow bandgap conjugated polymers pcpdtbt and pcdtpt," *Chemical Science*, vol. 7, no. 8, pp. 5313–5321, 2016.

[82] E. H. Suh, Y. J. Jeong, J. G. Oh, K. Lee, J. Jung, Y. S. Kang, and J. Jang, "Doping of donor–acceptor polymers with long side chains via solution mixing for advancing thermoelectric properties," *Nano Energy*, vol. 60, pp. 595–603, 2019.

[83] H.-R. Tseng, H. Phan, C. Luo, M. Wang, L. A. Perez, S. N. Patel, L. Ying, E. J. Kramer, T.-Q. Nguyen, G. C. Bazan, and A. J. Heeger, "High-mobility field-effect transistors fabricated with macroscopic aligned semiconducting polymers," *Advanced Materials*, vol. 26, no. 19, pp. 2993–2998, 2014.

[84] H. J. Cheon, T. S. Lee, J. E. Lee, S. B. Kim, E. H. Suh, S.-K. Kwon, Y. J. Jeong, J. Jang, and Y.-H. Kim, "Design of donor–acceptor polymer semiconductors for optimizing combinations with dopants to maximize thermoelectric performance," *Chemistry of Materials*, vol. 35, no. 4, pp. 1796–1805, 2023.

[85] L. Ying, B. B. Y. Hsu, H. Zhan, G. C. Welch, P. Zalar, L. A. Perez, E. J. Kramer, T.-Q. Nguyen, A. J. Heeger, W.-Y. Wong, and G. C. Bazan, "Regioregular pyridal[2,1,3]thiadiazole π-conjugated copolymers," *Journal of the American Chemical Society*, vol. 133, no. 46, pp. 18538–18541, 2011.

[86] M. Z. Iqbal, S. Khan, A. Rehman, S. S. Haider, M. A. Kamran, M. R. Abdul Karim, T. Alharbi, T. Hussain, S. Riaz, S. Naseem, and M. J. Iqbal, "Enhancement in the mobility of solution processable polymer based fet by incorporating graphene interlayer," *Superlattices and Microstructures*, vol. 137, p. 106331, 2020.

[87] H. Huang, Z. Chen, X. Chen, J. Jin, S. Huang, D. Wang, L. Wang, and D. Liu, "Substrate modification for high-performance thermoelectric materials and generators based on polymer and carbon nanotube composite," *Advanced Materials Interfaces*, 2022.

[88] X. Wu, S. Lan, D. Hu, Q. Chen, E. Li, Y. Yan, H. Chen, and T. Guo, "High performance flexible multilevel optical memory based on a vertical organic field effect transistor with ultrashort channel length," *Journal of Materials Chemistry C*, vol. 7, 2019.

[89] G. Zhang, J. Zhong, Q. Chen, Y. Yan, H. Chen, and T. Guo, "High-performance organic phototransistors with vertical structure design," *IEEE Transactions on Electron Devices*, vol. 66, no. 4, pp. 1815–1818, 2019.

[90] M. Azimi, A. Subramanian, N. A. Roslan, and F. Cicciora, "Flexible organic ion-gated transistors with low operating voltage and light-sensing application," *Journal of Physics: Materials*, vol. 4, no. 2, p. 024001, 2021.

[91] S. Song, S. Park, S. Kwon, B. H. Lee, J. A. Kim, S. H. Park, Y. Jin, J. Lee, I. Kim, K. Lee, and H. Suh, "Synthesis and characterization of phenanthrothiadiazole-based conjugated polymer for photovoltaic device," *Synthetic Metals*, vol. 162, no. 21–22, pp. 1936–1943, 2012.

[92] W. Zhong, S. Wang, and F. Liu, "Unlocking functional potentials: Nanofibril networks in organic semiconductors," *Advanced Nanocomposites*, vol. 2, pp. 124–147, December 2025.

[93] G. Acar, M. J. Iqbal, and M. U. Chaudhry, "Large area emission in p-type polymer-based light-emitting field-effect transistors by incorporating charge injection interlayers," *Materials*, vol. 14, no. 4, p. 901, 2021.

[94] J. Liang, Z. Song, S. Wang, X. Zhao, Y. Tong, H. Ren, S. Guo, Q. Tang, and Y. Liu, "Cobweb-like, ultrathin porous polymer films for ultrasensitive no2 detection," *ACS Applied Materials & Interfaces*, vol. 12, no. 47, pp. 52788–52796, 2020.

[95] G. Zhao, J. Sun, M. Zhang, S. Guo, X. Wang, J. Li, Y. Tong, X. Zhao, Q. Tang, and Y. Liu, "Highly strain-stable intrinsically stretchable olfactory sensors for imperceptible health monitoring," *Advanced Science*, vol. 10, no. 29, p. 2302974, 2023.

[96] J. I. Scott, X. Xue, M. Wang, R. J. Kline, B. C. Hoffman, and D. Dougherty, "Significantly increasing the ductility of high performance polymer semiconductors through polymer blending," *ACS Applied Materials & Interfaces*, vol. 8, no. 22, pp. 14037–14045, 2016.

[97] S. Guo, Y. Tong, X. Wang, M. Zhang, H. Yu, H. Ren, Q. Tang, G. Lu, and Y. Liu, "Brittle pcdtpt based elastic hybrid networks for transparent stretchable skin-like electronics," *Advanced Electronic Materials*, vol. 9, p. 2200438, 2023.

[98] H. Shan, J. He, Y. Yan, Y. Wang, J. Zhou, and H. Huo, "Electrical and mechanical properties of pcdtpt/sebs blend films driven by sebs microphase-separated structures and component concentrations," *Macromolecules*, vol. 58, no. 21, pp. 11731–11744, 2025.

[99] J. Kilby, "Invention of the integrated circuit," *IEEE Transactions on Electron Devices*, vol. 23, no. 7, pp. 648–654, 1976.

[100] H. Harris, "Concerning a thermometer with solid-state diodes," *Sci. Am*, vol. 204, p. 192, 1961.

[101] A. G. McNamara, "Semiconductor diodes and transistors as electrical thermometers," *Review of Scientific Instruments*, vol. 33, no. 3, pp. 330–333, 1962.

[102] R. C. Webb, A. P. Bonifas, A. Behnaz, Y. Zhang, K. J. Yu, H. Cheng, M. Shi, Z. Bian, Z. Liu, Y.-S. Kim, W.-H. Yeo, J. S. Park, J. Song, Y. Li, Y. Huang, A. M. Gorbach, and J. A. Rogers, "Ultrathin conformal devices for precise and continuous thermal characterization of human skin," *Nature Materials*, vol. 12, no. 10, pp. 938–944, 2013.

[103] M. Mansoor, I. Haneef, S. Akhtar, A. De Luca, and F. Udrea, "Silicon diode temperature sensors—a review of applications," *Sensors and Actuators A: Physical*, vol. 232, pp. 63–74, 2015.

[104] Q. Zhang, Y. Liu, H. Li, J. Wang, Y. Wang, F. Cheng, H. Han, and P. Zhang, "A review of sic sensor applications in high-temperature and radiation extreme environments," *Sensors*, vol. 24, no. 23, p. 7731, 2024.

[105] S. Santra, P. K. Guha, M. S. Haque, S. Z. Ali, and F. Udrea, "Si diode temperature sensor beyond 300°c," in *2007 International Semiconductor Conference*, vol. 2, pp. 415–418, 2007.

[106] A. De Luca, V. Pathirana, S. Z. Ali, D. Dragomirescu, and F. Udrea, "Experimental, analytical and numerical investigation of non-linearity of soi diode temperature sensors at extreme temperatures," *Sensors and Actuators A: Physical*, vol. 222, pp. 31–38, 2015.

[107] P. R. N. Childs, J. R. Greenwood, and C. A. Long, "Review of temperature measurement," *Review of Scientific Instruments*, vol. 71, no. 8, pp. 2959–2976, 2000.

[108] P. Mao, H. Li, and Z. Yu, "A review of skin-wearable sensors for non-invasive health monitoring applications," *Sensors*, vol. 23, no. 7, p. 3673, 2023.

[109] R. Roduit, P.-A. Besse, and J.-P. Micallef, "Flexible angular sensor [and biomechanical application]," *IEEE Transactions on Instrumentation and Measurement*, vol. 47, no. 4, pp. 1020–1022, 1998.

[110] L. Yan, Z. Liu, J. Wang, *et al.*, "Integrating hard silicon for high-performance soft electronics via geometry engineering," *Nano-Micro Letters*, vol. 17, p. 218, 2025.

[111] C. Wang, Z. Chen, C. L. J. Chan, Z. Wan, W. Ye, W. Tang, Z. Ma, B. Ren, D. Zhang, Z. Song, Y. Ding, Z. Long, S. Poddar, W. Zhang, Z. Wan, F. Xue, S. Ma, Q. Zhou, G. Lu, K. Liu, and Z. Fan, "Biomimetic olfactory chips based on large-scale monolithically integrated nanotube sensor arrays," *Nature Electronics*, vol. 7, pp. 157–167, 2024.

[112] S. Gupta, W. T. Navaraj, L. Lorenzelli, and R. S. Dahiya, "Ultra-thin chips for high-performance flexible electronics," *npj Flexible Electronics*, vol. 2, p. 8, 2018.

[113] T. Someya, T. Sekitani, S. Iba, Y. Kato, H. Kawaguchi, and T. Sakurai, "Conformable, flexible, large-area networks of pressure and thermal sensors with organic transistor active matrixes," *Proceedings of the National Academy of Sciences*, vol. 102, no. 35, pp. 12321–12325, 2005.

[114] L. Liu, Y. Dou, J. Wang, Y. Zhao, W. Kong, C. Ma, D. He, H. Wang, H. Zhang, A. Chang, and P. Zhao, "Recent advances in flexible temperature sensors: Materials, mechanism, fabrication, and applications," *Advanced Science*, vol. 11, no. 36, p. e2405003, 2024.

[115] J. Shin, B. Jeong, J. Kim, V. B. Nam, Y. Yoon, J. Jung, S. Hong, H. Lee, H. Eom, J. Yeo, J. Choi, D. Lee, and S. H. Ko, "Sensitive wearable temperature sensor with seamless monolithic integration," *Advanced Materials*, vol. 32, no. 2, p. 1905527, 2020.

[116] Z. Liu, B. Tian, Z. Jiang, S. Li, J. Lei, Z. Zhang, J. Liu, P. Shi, and Q. Lin, "Flexible temperature sensor with high sensitivity ranging from liquid nitrogen temperature to 1200 °c," *International Journal of Extreme Manufacturing*, vol. 5, no. 1, 2023.

[117] A. Köhler and H. Bässler, *Electronic Processes in Organic Semiconductors: An Introduction*. Weinheim: Wiley-VCH, 2015.

[118] Y. Huang, X. Chen, C. Zhang, Q. Peng, W. Huang, and P. K. L. Chan, "Effectively modulating thermal activated charge transport in organic semiconductors by precise potential barrier engineering," *Nature Communications*, vol. 12, no. 1, p. 2715, 2021.

[119] J. Guo, G. Li, H. Reith, L. Jiang, M. Wang, Y. Li, X. Wang, Z. Zeng, H. Zhao, X. Lu, G. Schierning, K. Nielsch, L. Liao, and Y. Hu, "Doping high-mobility donor–acceptor copolymer semiconductors with an organic salt for high-performance thermoelectric materials," *Advanced Electronic Materials*, vol. 6, no. 3, p. 1900945, 2020.

[120] X. Ren, P. K. L. Chan, J. Lu, B. Huang, and C. W. Leung, "High dynamic range organic temperature sensor," *Advanced Materials*, vol. 25, no. 9, pp. 1291–1295, 2013.

[121] H. Sun, Y. Xiao, Y. He, X. Wei, J. Zou, Y. Luo, Y. Wu, J. Zhao, V. K.-M. Au, and T. Yu, "3d printable organic room-temperature phosphorescent materials and printed real-time sensing and display devices," *Chemical Science*, vol. 16, pp. 5299–5307, 2025.

[122] Q. Di, L. Li, X. Miao, *et al.*, "Fluorescence-based thermal sensing with elastic organic crystals," *Nature Communications*, vol. 13, p. 5280, 2022.

[123] C. Si, T. Wang, A. K. Gupta, D. B. Cordes, A. M. Z. Slawin, J. S. Siegel, and E. Zysman-Colman, "Room-temperature multiple phosphorescence from functionalized corannulenes: Temperature sensing and afterglow organic light-emitting diode," *Angewandte Chemie International Edition*, vol. 62, no. 43, p. e202309718, 2023.

[124] S. Liu, K. Wang, S. Ke, M. Chen, X. Qian, X. Qin, L. Yin, Q. Fan, and Y. Qian, "Organic high-temperature sensing films based on esipt material," *Sensors and Actuators A: Physical*, vol. 377, p. 115757, 2024.

[125] T. Q. Trung and N. H. Lee, "Flexible and stretchable physical sensor integrated platforms for wearable human-activity monitoring and personal healthcare," *Advanced Materials*, vol. 28, no. 22, pp. 4338–4372, 2016.

[126] C. Wang, X. Liang, Z. Wang, and Z. Yin, "Advanced electronic skin devices for healthcare applications," *Journal of Materials Chemistry B*, vol. 8, no. 4, pp. 642–658, 2020.

[127] R. Zhang, Y. Liu, H. Chen, M. Wang, J. Li, D. Xu, L. Sun, and W. Zhou, "Self-powered intelligent tactile-sensing system based on organic electrochemical transistors," *ACS Applied Electronic Materials*, vol. 6, no. 5, pp. 2103–2112, 2024.

[128] S. Chen, Z. Zhou, K. Hou, Y. Li, X. Wang, L. Zhang, J. Liu, Y. Wu, F. Yang, H. Zhao, J. Xu, Y. Liu, Z. Wang, X. Li, and Q. Sun, "Artificial organic afferent nerves enable closed-loop tactile feedback for intelligent robot," *Nature Communications*, vol. 15, no. 1, p. 7056, 2024.

[129] L. Liu, Y. Dou, J. Wang, Y. Zhao, W. Kong, C. Ma, D. He, H. Wang, H. Zhang, A. Chang, and P. Zhao, "Recent advances in flexible temperature sensors: Materials, mechanism, fabrication, and applications," *Advanced Science*, vol. 11, no. 30, p. 2405003, 2024.

[130] Y. Liu, J. Wang, T. Liu, Z. Wei, B. Luo, M. Chi, S. Zhang, C. Cai, C. Gao, T. Zhao, S. Wang, and S. Nie, "Triboelectric tactile sensor for pressure and temperature sensing in high-temperature applications," *Nature Communications*, vol. 16, no. 1, p. 383, 2025.

[131] S. Hao, F. Wang, J. Guan, K. Tang, and X. Wang, "Skin temperature indexes to evaluate thermal sensation and cognitive performance in hot environments," *Building and Environment*, vol. 236, p. 110354, 2023.

[132] T. G. Brooks, N. F. Lahens, G. R. Grant, Y. I. Sheline, G. A. FitzGerald, and C. Skarke, "Diurnal rhythms of wrist temperature are associated with future disease risk in the uk biobank," *Nature Communications*, vol. 14, 2023.

[133] C. Stefanadis, C. Chrysohoou, D. B. Panagiotakos, E. Passalidou, V. Katsi, V. Polychronopoulos, and P. K. Toutouzas, "Temperature differences are associated with malignancy on lung lesions: a clinical study," *BMC Cancer*, vol. 3, no. 1, pp. 1–5, 2003.

[134] "An analysis of tumor-related skin temperature differences in malignant soft-tissue tumors," *Journal of Orthopaedic Science*, vol. 27, pp. 234–243, 2022. Access provided by University of Durham Main Library.

[135] Y. Khan, A. E. Ostfeld, C. M. Lochner, A. Pierre, and A. C. Arias, "Monitoring of vital signs with flexible and wearable medical devices," *Advanced Materials*, vol. 28, no. 22, pp. 4373–4395, 2016.

[136] Z. Hu, M. Cui, and X. Wu, "Real-time temperature prediction of power devices using an improved thermal equivalent circuit model and application in power electronics," *Micromachines*, vol. 15, no. 1, p. 63, 2024.

[137] R. Hercík, M. Mikolajek, R. Byrtus, S. Hejduk, J. Látal, A. Vanderka, Z. Macháček, and J. Koziorek, "Construction of a high-temperature sensor for industry based on optical fibers and ruby crystal," *Sensors*, vol. 24, no. 12, p. 3703, 2024.

[138] T. Jeyaseelan, P. Ekambaram, J. Subramanian, and T. Shamim, "A comprehensive review on the current trends, challenges and future prospects for sustainable mobility," *Renewable and Sustainable Energy Reviews*, vol. 157, p. 112073, 2022.

[139] Y. Zhang, J. Jin, Y. Zhang, D. Mei, and Y. Wang, "Flexible temperature sensor with wide sensing range and fast response enabled by pedot:pss/cnt and thermal management encapsulation," *ACS Applied Electronic Materials*, vol. 7, no. 13, pp. 5981–5993, 2025.

[140] Y. Qian, X. Zhang, L. Xie, D. Qi, B. K. Chandran, and X. Chen, "Stretchable organic semiconductor devices," *Advanced Materials*, vol. 28, no. 44, pp. 9243–9265, 2016.

[141] M. L. Hammock, A. Chortos, B. C. K. Tee, J. B.-H. Tok, and Z. Bao, "25th anniversary article: The evolution of electronic skin (e-skin): A brief history, design considerations, and recent progress," *Advanced Materials*, vol. 25, no. 42, pp. 5997–6038, 2013.

[142] D. Elkington, N. Cooling, W. Belcher, P. Dastoor, and X. Zhou, "Organic thin-film transistor (otft)-based sensors," *Electronics*, vol. 3, no. 2, pp. 234–254, 2014.

[143] S. Harada, K. Kanao, Y. Yamamoto, T. Arie, S. Akita, and K. Takei, "Fully printed flexible fingerprint-like three-axis tactile and slip force and temperature sensors for artificial skin," *ACS Nano*, vol. 8, no. 12, pp. 12851–12857, 2014.

[144] Y. Su, C. Ma, J. Chen, and et al., "Printable, highly sensitive flexible temperature sensors for human body temperature monitoring: A review," *Nanoscale Research Letters*, vol. 15, p. 234, 2020.

[145] X. Wu, S. Mao, J. Chen, and J. Huang, "Strategies for improving the performance of sensors based on organic field-effect transistors," *Advanced Materials*, vol. 30, no. 6, p. 1705642, 2018. First published: 29 January 2018.

[146] A. Kumar, P. K. Bhatnagar, P. C. Mathur, *et al.*, "Temperature and electric-field dependence of hole mobility in light-emitting diodes based on poly[2-methoxy-5-(2-ethylhexoxy)-1,4-phenylene vinylene]," *Journal of Applied Physics*, vol. 98, no. 2, p. 024502, 2005.

[147] A. M. Ganose, J. Park, and A. Jain, "The temperature-dependence of carrier mobility is not a reliable indicator of the dominant scattering mechanism," *arXiv*, 2022.

[148] V. Podzorov, S. E. Sysoev, E. Loginova, V. M. Pudalov, and M. E. Gershenson, "Intrinsic charge transport on the surface of organic semiconductors," *Physical Review Letters*, vol. 93, no. 8, p. 086602, 2004.

[149] X. Wang, L. Dong, H. Zhang, R. Yu, C. Pan, and Z. L. Wang, "Recent progress in electronic skin," *Advanced Science*, vol. 2, no. 10, p. 1500169, 2015.

[150] W. Gao, S. Emaminejad, H. Y. Y. Nyein, S. Challa, K. Chen, A. Peck, H. M. Fahad, H. Ota, H. Shiraki, D. Kiriya, D.-H. Lien, G. A. Brooks, R. W. Davis, and A. Javey, "Fully integrated wearable sensor arrays for multiplexed in situ perspiration analysis," *Nature*, vol. 529, pp. 509–514, 2016.

[151] M. C. J. M. Vissenberg and M. Matters, "Theory of the field-effect mobility in amorphous organic transistors," *Physical Review B*, vol. 57, no. 20, pp. 12964–12967, 1998.

[152] I. McCulloch, M. Heeney, C. Bailey, K. Genevicius, I. Macdonald, M. Shkunov, D. Sparrowe, S. Tierney, R. Wagner, W. Zhang, M. L. Chabinyc, R. J. Kline, M. D. McGehee, and M. F. Toney, "Liquid-crystalline semiconducting polymers with high charge-carrier mobility," *Nature Materials*, vol. 5, pp. 328–333, 2006.

[153] T. O. Boucher, *Computer Automation in Manufacturing: An Introduction*. Springer Science & Business Media, 2012.

[154] H. Prajapati and N. N. Deshmukh, "Design and development of thin wire sensor for transient temperature measurement," *Measurement*, vol. 140, pp. 582–589, 2019.

[155] R. F. Pierret, *Semiconductor Device Fundamentals*. Addison-Wesley, 1996.

[156] S. Majumder, T. Mondal, and M. J. Deen, "Wearable sensors for remote health monitoring," *Sensors*, vol. 17, no. 1, 2017.

[157] S. Bielska, M. Sibinski, and A. Lukasik, "Polymer temperature sensor for textronic applications," *Materials Science and Engineering: B*, vol. 165, pp. 50–52, 2009.

[158] A. Grafa, M. Arndt, and G. Gerlach, "Seebeck's effect in micromachined thermopiles for infrared detection: A review," *Proceedings of the Estonian Academy of Sciences. Engineering*, vol. 13, pp. 338–353, 2007.

[159] P. R. N. Childs, "5 - thermocouples," in *Practical Temperature Measurement* (P. R. N. Childs, ed.), pp. 98–144, Oxford: Butterworth-Heinemann, 2001.

[160] H. S. Lee, *Thermal Design: Heat Sinks, Thermoelectrics, Heat Pipes, Compact Heat Exchangers, and Solar Cells*. Hoboken, NJ: John Wiley & Sons, 2010.

[161] Y. Zhang, H. Wang, L. Guo, W. Liu, and Z. Wang, "Influences of rf magnetron sputtering power and gas flow rate on a high conductivity and low drift rate of tungsten–rhenium thin-film thermocouples," *Nanomaterials*, vol. 12, no. 7, p. 1120, 2022.

[162] G. Gao, Y. Zhang, H. Wang, W. Liu, and Z. Wang, "Influences of rf magnetron sputtering power and gas flow rate on a high conductivity and low drift rate of tungsten–rhenium thin-film thermocouples," *Coatings*, vol. 13, no. 8, p. 1405, 2023.

[163] X. P. V. Maldague, *Theory and Practice of Infrared Technology for Nondestructive Testing*. New York, NY, USA: Wiley, 2001.

[164] M. F. Modest, *Radiative Heat Transfer*. Waltham, MA, USA: Academic Press, 3rd ed., 2013.

[165] C. Meola and G. M. Carlomagno, "Recent advances in the use of infrared thermography," *Measurement Science and Technology*, vol. 15, no. 9, pp. R27–R58, 2004.

[166] F. Ciampa, P. Mahmoodi, F. Pinto, and M. Meo, "Recent advances in active infrared thermography for non-destructive testing of aerospace components," *Sensors*, vol. 18, no. 2, p. 609, 2018.

[167] C. Soutis, "Fibre reinforced composites in aircraft construction," *Progress in Aerospace Sciences*, vol. 41, no. 2, pp. 143–151, 2005.

[168] A. Allouhi, A. Boharb, R. Saidur, T. Kousksou, and A. Jamil, "5.1 energy auditing," in *Comprehensive Energy Systems* (I. Dincer, ed.), pp. 1–44, Oxford: Elsevier, 2018.

[169] B. Lahiri, S. Bagavathiappan, T. Jayakumar, and J. Philip, "Medical applications of infrared thermography: A review," *Infrared Physics & Technology*, vol. 55, no. 3, pp. 221–235, 2020.

[170] X. Cao and Y. Han, "Control over the aggregated structure of donor–acceptor conjugated polymer films for high-mobility organic field-effect transistors," *Aggregate*, vol. 5, no. 3, p. 501, 2024.

[171] E. K. Lee, M. Y. Lee, C. H. Park, H. R. Lee, and J. H. Oh, "Toward environmentally robust organic electronics: Approaches and applications," *Advanced Materials*, vol. 29, no. 44, p. 1703638, 2017.

[172] K. Norrman, A. Ghanbari-Siahkali, and N. B. Larsen, "6 studies of spin-coated polymer films," *Annual Reports on the Progress of Chemistry. Section C: Physical Chemistry*, vol. 101, pp. 174–201, 2005.

[173] L. Xu, J. Yang, K. Li, L. Yang, and J. Zhu, "Effect of post-deposition annealing on the structural evolution and optoelectronic properties of in_2o_3:h thin films," *Nanomaterials*, vol. 12, no. 19, p. 3533, 2022.

[174] H.-C. Liao, M.-H. Jao, Y.-H. Chen, Y.-Y. Lai, and S.-A. Chen, "Insights into solvent vapor annealing on the performance of bulk heterojunction solar cells by a quantitative nanomorphology study," *RSC Advances*, vol. 4, no. 12, pp. 6382–6388, 2014.

[175] D. M. Taylor, "Vacuum-thermal-evaporation: the route for roll-to-roll production of large-area organic electronic circuits," *Semiconductor Science and Technology*, vol. 30, no. 5, p. 054002, 2015.

[176] Y. Chen, B. Lu, Y. Chen, and X. Feng, "Breathable and stretchable temperature sensors inspired by skin," *Scientific Reports*, vol. 5, p. 11505, 2015.

[177] C.-Y. Lee, F.-B. Weng, C.-H. Cheng, H.-R. Shiu, S.-P. Jung, W.-C. Chang, P.-C. Chan, W.-T. Chen, and C.-J. Lee, "Use of flexible micro-temperature sensor to determine temperature in situ and to simulate a proton exchange membrane fuel cell," *Journal of Power Sources*, vol. 196, no. 1, pp. 228–234, 2011.

[178] C.-C. Huang, Z.-K. Kao, and Y.-C. Liao, "Flexible miniaturized nickel oxide thermistor arrays via inkjet printing technology," *ACS Applied Materials & Interfaces*, vol. 5, no. 24, pp. 12954–12959, 2013.

[179] K. Felmet, Y. Loo, and Y. Sun, "Patterning conductive copper by nanotransfer printing," *Applied Physics Letters*, vol. 85, no. 16, pp. 3316–3318, 2004.

[180] W.-H. Yeo, Y. S. Kim, J. Lee, A. Ameen, L. Shi, M. Li, S. Wang, R. Ma, S.-H. Jin, Z. Kang, Y. Huang, and J. A. Rogers, "Multifunctional epidermal electronics printed directly onto the skin," *Advanced Materials*, vol. 25, no. 20, pp. 2773–2778, 2013.

[181] S. Yoon, J. K. Sim, and Y.-H. Cho, "A flexible and wearable human stress monitoring patch," *Scientific Reports*, vol. 6, p. 23468, 2016.

[182] A. Gibaud, M. Chebil, and T. Beauvier, "X-ray reflectivity," in *Surface Science Techniques* (G. Bracco and B. Holst, eds.), pp. 191–216, Berlin, Heidelberg: Springer, 2013.

[183] J. Tiilikainen, J.-M. Tilli, V. Bosund, M. Mattila, T. Hakkarainen, J. Sormunen, and H. Lipsanen, "Accuracy in x-ray reflectivity analysis," *Journal of Physics D: Applied Physics*, vol. 40, no. 23, pp. 7497–7503, 2007.

[184] Wikipedia contributors, "X-ray reflectivity." `https://en.wikipedia.org/wiki/X-ray_reflectivity`, 2024.

[185] A. Kossoy, V. Merk, D. Simakov, K. Leosson, S. Kéna-Cohen, and S. A. Maier, "State of the art of ultra-thin gold layers: formation fundamentals and implications," *Nanoscale Advances*, vol. 4, pp. 1080–1094, 2022.

[186] J. Als-Nielsen and D. McMorrow, *Elements of Modern X-Ray Physics*. Wiley, 2 ed., 2011.

[187] I. Sachs, M. Fuhrmann, W. Deferme, and H. Möbius, "Determination of layer morphology of rough layers in organic light emitting diodes by x-ray reflectivity," *Engineering Reports*, vol. 5, no. 4, p. e12594, 2023.

[188] V. Holý and T. Baumbach, "Nonspecular x-ray reflection from rough multilayers," *Physical Review B*, vol. 49, pp. 10668–10676, 1994.

[189] L. G. Parratt, "Surface studies of solids by total reflection of x-rays," *Physical Review*, vol. 95, pp. 359–369, 1954.

[190] Y. Fujii, "Recent developments in the x-ray reflectivity analysis for rough surfaces and interfaces of multilayered thin film materials," *Journal of Materials*, vol. 2013, p. 678361, 2013.

[191] Y. Fujii, "Improvement of surface and interface roughness estimation on x-ray reflectivity," *Powder Diffraction*, vol. 29, no. 3, pp. 265–268, 2014.

[192] T. H. Le, Y. Kim, and H. Yoon, "Electrical and electrochemical properties of conducting polymers," *Polymers*, vol. 9, p. 150, Apr 2017.

[193] A. Salleo, T. W. Chen, A. R. Völkel, Y. Wu, P. Liu, B. S. Ong, and R. A. Street, "Intrinsic hole mobility and trapping in a regioregular poly(thiophene)," *Physical Review B*, vol. 70, p. 115311, 2004.

[194] H. Sirringhaus, "Device physics of solution-processed organic field-effect transistors," *Advanced Materials*, vol. 17, pp. 2411–2425, 2005.